# Nuclear Data and Experiments for Astrophysics 4

Anu Kankainen and Stephane Goriely

**Abstract**

Nuclear astrophysics aims to understand the origin of elements and the role of nuclear processes in astrophysical events. Nuclear reactions and reaction rates depend strongly on nuclear properties and on the astrophysical environment. Nuclear inputs for stellar reaction rates involve a variety of nuclear properties, theoretical models, and experimental data. Experiments providing data for nuclear astrophysics range from stable ion beam direct measurements to radioactive beam experiments employing inverse kinematics or indirect methods. Many properties relevant for astrophysical calculations, such as nuclear masses and $\beta$-decays, have also been intensively studied. This contribution shortly introduces selected astrophysical processes, discusses the related nuclear data needs, and gives examples of recent experimental and theoretical efforts in the field.

## 4.1 Origin of Elements and Nucleosynthesis Processes

### 4.1.1 The Composition of the Universe

Our knowledge of the composition of the Universe in general, and of our Solar System in particular, results almost entirely from the analysis of electromagnetic spectra originating from the various observable sources in the Universe, i.e., the

A. Kankainen (✉)
Department of Physics, University of Jyväskylä, Jyväskylä, Finland
e-mail: anu.kankainen@jyu.fi

S. Goriely
Institut d'Astronomie et d'Astrophysique, Université Libre de Bruxelles, Brussels, Belgium
e-mail: sgoriely@astro.ulb.ac.be



S. M. Lenzi, D. Cortina-Gil (eds.), *The Euroschool on Exotic Beams, Vol. VI*,
Lecture Notes in Physics 1005, https://doi.org/10.1007/978-3-031-10751-1_4

galaxies, the interstellar medium, and the stars of all types (including first of all, our sun) but also from the minute portion of matter which is accessible to the human kind, i.e., meteorites, planets (the Earth and the Moon in particular), energetic solar particles, and the galactic as well as extra galactic cosmic rays. Information provided by such sources on the present composition of the Universe can be found in Refs. [1–4].

One of the fundamental developments resulting from the various observations performed for the last decades is found in the determination of the composition of our own Solar System at the time of its formation some 4.6 billion years ago [5–8]. It is principally based on a special class of meteorites called carbonaceous chondrites of type CI1, considered as the most unaffected sample of matter accessible to man and representative of the primitive solar material. The analysis of the solar spectrum is in good agreement with the meteorite analysis and helps in addition to determine the abundances of some volatile elements, such as H, He, C, N, O, and Ne, which cannot be measured in meteorites reliably. In some cases (Ar, Kr, Xe, Hg), it remains difficult to extract accurate abundances from observational data, and some theoretical consideration is then required. From the primitive solar composition, it is possible to understand the differences observed today in the various constituents of the Solar System calling for the numerous physico-chemical and geological processes having taken place for the last 4.6 billion years. If the elementary composition appears relatively diversified among the various constituents of the Solar System, a very high homogeneity of the isotopic composition is found. For this reason, the isotopic composition of the terrestrial matter is generally used to determine the abundance of the nuclides in the Solar System. The resulting abundance distribution is shown in Fig. 4.1.

Figure 4.1 presents some interesting features. In particular, H and He are the most abundant species in the Solar System. In contrast, Li, Be, and B are extremely underabundant in comparison with the neighboring elements. For nuclei heavier than C, the abundances decrease with increasing atomic numbers $A$. On top of this general decreasing trend, there are superimposed abundance peaks, with the most prominent peak found for Fe. For $A \leq 56$, secondary peaks every multiple of 4 can be seen, while above Fe a large peak is observed around $80 \leq A \leq 90$ and two double peaks at $A = 130$–$138$ and $A = 195$–$208$. In the $A \gtrsim 50$ region, the abundances are also characterized by a saw feature. Such features, as well as the other remarkable features seen in Fig. 4.1, have been recognized since the early analysis of these curves as bearing the signature of specific nuclear properties.

For practical reasons, but also to highlight the link between observations and nucleosynthesis models, it is of particular relevance to divide the abundance curve of the elements heavier than iron into three distributions associated with the stable nuclides located at the bottom of the valley of $\beta$-stability, on the neutron-rich side of the valley, and on the neutron-deficient side. For even values of $A$, many isobars can exist; in this case, the stable most neutron-rich isobar is called r-nucleus and the most proton-rich p-nucleus. The s-nuclei are located between these two isobars, (i.e., at the bottom of the valley). When only one isobar exists, it is usually classified as an sr mix nucleus. The actinides are considered as being of r type. This denomination

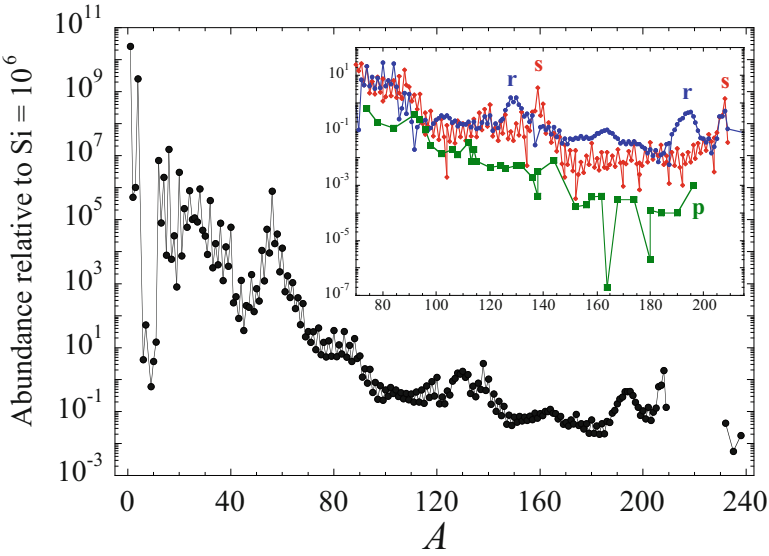


**Fig. 4.1** Distribution of isotopic abundances characteristic of our Solar System at the time of formation [7]. The insert shows the decomposition of the Solar System distribution into the s-, r-, and p-abundances for elements heavier than iron [9–11]

is strongly related to the identification of the different mechanisms responsible for the production of the s-, r-, and p-nuclei, i.e., the so-called s-process (for slow), r-process (for rapid), and p-process (for proton). After performing such a nuclear decomposition (see, e.g., [9]), it is found that the double peak structure observed in Fig. 4.1 is now divided into two components, the "heavy" peaks at $A = 138$ and $A = 208$ attributed to the s-process and the "light" r-process peaks at $A = 130$ and $A = 195$ (see Fig. 4.1). The p-nuclei are in contrast about 100–1000 times less abundant than their s and r isobaric counterparts.

Let us finally mention that if the bulk of the Solar System material is found to be of a very high isotopic homogeneity, a small portion of this material ($\lesssim 10^{-4} M_\odot$, where $M_\odot$ is the mass of the Sun) is characterized by a variety of more or less different isotopic compositions. These so-called isotopic anomalies are observed either in meteoritic material which condensed in the solar nebula or in grains probably of circumstellar origins. These grains were formed around stars of various types and survived the protosolar nebula and their inclusion within meteorites. While the Solar System composition illustrated in Fig. 4.1 is considered as resulting from a perfect mix of the ashes produced by a large number of nucleosynthetic events that took place in the Galaxy during the $\sim 10^{10}$ years preceding the Solar System formation, the isotopic anomalies are believed to be caused by a relative small number of events. The analysis of some anomalies due to the in situ radioactive decay of short-lived nuclides (with half-lives of $10^5 \lesssim t_{1/2} \lesssim 10^8$ yr) can even provide severe constraints on the time elapsed between their production

and their injection in the Solar System in formation. More information on the isotopic anomalies can be found in the review papers [12–14].

The Solar System is the object of the Universe that provides us with the most complete set of observational data concerning the elements and isotopes abundances. A myriad of information exists nevertheless on the composition of other objects which emphasizes features similar to our solar abundances, as well as a large diversity. Diversity is found not only among objects belonging to different classes but also among objects of the same type. In particular, the abundances observed at the stellar surface can vary with the age of the star, its location in the Galaxy, or its spectral type. Two major effects are found responsible for this abundance diversity: stellar evolution and the chemical evolution of the Galaxy.

### 4.1.2 Nucleosynthesis Models

One of the most fundamental questions astrophysics tries to answer concerns the present and past composition of the Universe and of its many constituents. The theory of nucleosynthesis aims at identifying the various processes that can be invoked to explain the origin of the nuclides observed in nature, as well as the astrophysical sites capable of providing the conditions required for these processes to take place. The works of [15, 16] represent milestone in this field.

Nuclear reactions represent the fundamental ingredients of all nucleosynthesis models. Two major classes of nuclear reactions are invoked: the thermonuclear reactions and the non-thermal transformations also known as spallation reactions. Thermonuclear reactions took place at the level of the primordial or cosmological (Big Bang) level as well as inside the stars all along the galactic evolution up to date. On the other hand, spallation reactions are important in diluted and cold medium, as the interstellar medium, through the interaction with galactic cosmic rays (GCRs), and at the surface of stars or in their surroundings through interaction with energetic stellar particles [17].

The primordial Big Bang nucleosynthesis (BBN) is responsible for the bulk He content of the Universe as well as for the synthesis of some other nuclei, like D, $^{3}$He, and $^{7}$Li. All the other nuclides, as well as a fraction of the galactic $^{7}$Li, and maybe $^{3}$He, result from thermonuclear reactions taking place inside the stars. The only exceptions concern the $^{6}$Li, Be, and B nuclei for which spallation reactions from the nuclear interaction of GCRs (accelerated CNO nuclei) with the interstellar medium (mainly protons and $\alpha$-particles) are invoked [17].

In stars, the thermonuclear reactions can be induced by charged particles (proton or $\alpha$-particles) or neutrons. In the former case, the reactions mainly take place on light or medium heavy nuclei $A \lesssim 60$–$70$, since the reactions involving heavier species are not probable enough (because of the too high Coulomb barrier) to play a significant role in realistic stellar environments (cf. Sect. 4.2). The importance of the charged particle-induced reactions is twofold. First, they are fundamental for the energy production enabling the star to counterbalance its energy loss (energetic equilibrium), and second, they locally modify the stellar content where they take

place. The neutron-induced reactions are obviously not restricted to species lighter than Fe, since no Coulomb barrier exists in this case. However, these reactions never contribute to the nuclear energy production.

The origin of most of the elements lighter than those of the Fe group has been explained, mainly thanks to the direct link between their nucleosynthesis and the energetic evolution of stars [18–20]. However, the synthesis of nuclei heavier than Fe is far from being well understood at the present time. The major mechanisms called for to explain the production of the heavy nuclei are the slow neutron-capture process (or s-process), occurring during hydrostatic stellar burning phases, the rapid neutron-capture process (or r-process) believed to develop during the explosion of a star as a supernova or during the coalescence of two-neutron stars (NSs) or a NS and a black hole (BH) in a binary system, and the p-process occurring in core-collapse supernova (CCSN) or Type Ia supernovae (SNIa). Recently, an intermediate neutron-capture process (or i-process) has also been proposed to explain observed abundances in low-metallicity stars. More information on these four nucleosynthesis processes is given in Fig. 4.2 and below.

#### 4.1.2.1 The s-Process

For the last decades, an extremely intense amount of work has been devoted to the s-process of nucleosynthesis called to explain the origin of the stable nuclides heavier than iron located at the bottom of the valley of nuclear stability [22–25].

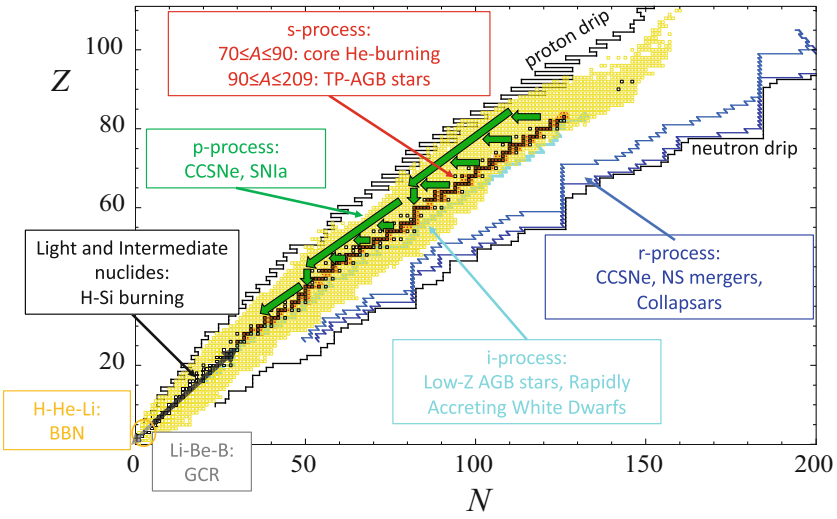


**Fig. 4.2** Schematic representation in the $(N, Z)$ plane of the different astrophysical sites responsible for the synthesis of the stable nuclides. The nucleosynthetic contributions by BBN and by GCR are also displayed. The open black squares correspond to stable or long-lived nuclei, and the open yellow squares to the nuclei with experimentally known masses [21]. Nuclei with neutron or proton separation energies tending to zero define the neutron or proton "drip lines" (solid black lines), as predicted from a mass model. More details can be found in [4] (Modified from Ref. [4])

Even though the observation of the radioactive Tc in stellar envelopes clearly proves that the s-process takes place during hydrostatic burning phases of a star, it remains difficult to explain the origin of the large neutron concentrations required to produce s-elements. Two nuclear reactions are suggested as possible neutron sources, i.e., $^{13}$C($\alpha$,n)$^{16}$O and $^{22}$Ne($\alpha$,n)$^{25}$Mg. These reactions could be responsible for a large production of neutrons during given burning phases, namely, the core He-burning of massive stars (heavier than 10 $M_{\odot}$) and the shell He-burning during the thermal asymptotic giant branch (AGB) instabilities well-known as thermal pulses (TP) of low- and intermediate-mass stars (lower than typically 10 $M_{\odot}$).

As reviewed in great detail by Karakas and Lattanzio [24], the s-process in AGB stars is thought to occur in their He-burning shell surrounding an inert C-O core, either during recurrent and short convective TP episodes or in between these pulses. A rather large diversity of s-nuclide abundance distributions are predicted to be produced. A fraction of the synthesized s-nuclides (along with other He-burning products) could then be dredged up to the surface shortly after each pulse. In low-mass AGB stars (less than 3 $M_{\odot}$), it is generally considered that the necessary neutrons for the development of the s-process are mainly provided by $^{13}$C($\alpha$,n)$^{16}$O, which can operate at temperatures around (1$\sim$1.5) $\times$ $10^8$ K. The efficiency of this mechanism is predicted to be the highest in stars with metallicities [Fe/H] lower than solar ([Fe/H] $\ll$ 0). The astrophysical models underlying the thermal pulse scenario are still quite uncertain, in particular in the description of the mechanisms that could be at the origin of the neutron production. The neutron production in these locations depends sensitively on the mechanism of proton ingestion into underlying He-rich layers in amounts and at temperatures that allow the operation of the $^{12}$C(p,$\gamma$)$^{13}$N($\beta^+$)$^{13}$C($\alpha$,n)$^{16}$O, while the production of $^{14}$N by $^{13}$C(p,$\gamma$)$^{14}$N is inefficient enough to avoid the hold-up of neutrons by the $^{14}$N neutron poison. TP-AGB models including empirical diffusive overshoot have been relatively successful to explain such a partial mixing of protons from the H-rich envelope into the C-rich layers during the third dredge-up [24, 25], but it remains difficult to model such mixing mechanisms in common one-dimensional models.

Massive stars, and more specifically their He-burning cores and, to some extent, their C-burning shells, are also predicted to be s-nuclide producers through the operation of the $^{22}$Ne($\alpha$,n)$^{25}$Mg reaction. This neutron source can indeed be active in these locations that are hotter than the He shell of AGB stars. In addition, $^{22}$Ne burning can also be activated in the C-burning shell of massive stars. Many calculations performed in the framework of realistic stellar models come to the classical conclusion that this site is responsible for a substantial production of the 70 $\lesssim$ $A$ $\lesssim$ 90 s-nuclides and can in particular account for the Solar System abundances of these species. It has also been shown that rotation can significantly increase the efficiency of the s-process, especially at low metallicity [26–28]. Because of the rotational mixing operating between the H-shell and He-core during the core helium burning phase, the abundant $^{12}$C and $^{16}$O isotopes in the convective He-burning core are mixed within the H-shell, boosting the CNO cycle and forming primary $^{14}$N that finally leads to the synthesis of extra $^{22}$Ne, hence an increased neutron production.

#### 4.1.2.2 The r-Process

The r-process of stellar nucleosynthesis is called for to explain the production of the stable (and some long-lived radioactive) neutron-rich nuclides heavier than iron that are observed in stars of various metallicities, as well as in the Solar System. Reviews can be found in Refs. [4, 11, 29].

Nuclear physics-based and astrophysics-free r-process models of different levels of sophistication have been constructed over the years. They all have their merits and their shortcomings. The ultimate goal was to identify realistic sites for the development of the r-process. For long, the core-collapse supernova of massive stars has been envisioned as the privileged r-process location. One- or multi-dimensional spherical or aspherical explosion simulations in connection with the r-process nucleosynthesis are reviewed in Refs. [4, 11, 29]. Progress in the modeling of type II supernovae and $\gamma$-ray bursts has raised a lot of excitement about the so-called neutrino-driven wind environment. However, until now a successful r-process cannot be obtained ab initio without tuning the relevant parameters (neutron excess, entropy, expansion timescale) in a way that is not supported by the most sophisticated existing models [30, 31]. Although these scenarios remain promising, especially in view of their potential to contribute to the galactic enrichment significantly, they remain affected by large uncertainties associated mainly with the still incompletely understood mechanism responsible for the supernova explosion and the persistent difficulties to obtain suitable r-process conditions in self-consistent dynamical explosion and NS cooling models [30, 32, 33]. In particular, a subclass of CCSNe, the so-called collapsars, corresponding to the fate of rapidly rotating and highly magnetized massive stars and generally considered to be at the origin of observed long $\gamma$-ray bursts, could be a promising r-process site [34–36]. The production of r-nuclides in these events may be associated with jets predicted to accompany the explosion or with the accretion disk formed around a newly born central BH [37].

Since early 2000s, special attention has been paid to NS mergers as r-process sites following the confirmation by hydrodynamic simulations that a non-negligible amount of matter could be ejected from the system. Newtonian [38], conformally flat general relativistic [39, 40], as well as fully relativistic [41, 42] hydrodynamic simulations of NS-NS and NS-BH mergers with microphysical equations of state have demonstrated that typically some $10^{-3}\,M_\odot$ up to more than $0.1\,M_\odot$ can become gravitationally unbound on roughly dynamical timescales due to shock acceleration and tidal stripping. Also the relic object (a hot, transiently stable hypermassive NS followed by a stable supermassive NS, or a BH-torus system), can lose mass through outflows driven by a variety of mechanisms [40].

Simulations of growing sophistication have confirmed that the ejecta from NS mergers are viable strong r-process sites up to the third abundance peak and the actinides. The r-nuclide enrichment is predicted to originate both from the dynamical (prompt) material expelled during the NS-NS or NS-BH merger phase and from the outflows generated during the post-merger remnant evolution of the relic BH-torus system. The resulting abundance distributions are found to reproduce

very well the Solar System distribution, as well as various elemental distributions observed in low-metallicity stars [29]. In addition, the ejected mass of r-process material, combined with the predicted astrophysical event rate (around $10\,\mathrm{My}^{-1}$ in the Milky Way) can account for the majority of r-material in our Galaxy. A further piece of evidence that NS mergers are r-nuclide producers indeed comes from the very important 2017 gravitational wave and electromagnetic observation of the kilonova GW170817 [43, 44].

Despite the recent success of nucleosynthesis studies for NS mergers, the details of r-processing in these events are still affected by a variety of uncertainties, both from the nuclear physics and astrophysics point of view. In particular, it has been shown that weak interactions may strongly affect the composition of the dynamical ejecta and thus the efficiency of the r-process [42, 45–47].

The r-process nucleosynthesis is also important for understanding the origin of the radionuclides that could be used to estimate an approximate age of the Galaxy, the so-called radio-cosmochronometers. The stellar production of heavy elements requires a detailed knowledge not only of the astrophysical sites and physical conditions in which the processes take place but also of the chemical evolution of the Galaxy.

#### 4.1.2.3 The i-Process

The s- and r-processes introduced very early in the development of the theory of nucleosynthesis have to be considered as the end members of a whole class of neutron-capture mechanisms. Supported by some observations that were difficult to reconcile solely with a combination of the s- and r-processes, a process referred to nowadays as an intermediate or i-process has been put forth, with neutron concentrations in the approximate $10^{12}$ to $10^{16}$ neutrons/cm$^3$ range. The mechanism envisaged to be responsible for this production is the ingestion of protons in He- and C-rich layers, leading to the production of $^{13}$C through $^{12}\mathrm{C(p,}\gamma)^{13}\mathrm{N}(\beta^+)^{13}\mathrm{C}$ followed by a substantial production of neutrons through $^{13}\mathrm{C}(\alpha,\mathrm{n})^{16}\mathrm{O}$. This is analogous to the mechanism already considered to be active in TP-AGB stars (Sect. 4.1.2.1), but the higher neutron concentrations are expected to result from the very low metallicity of the considered stars and the activation of $^{13}\mathrm{C}(\alpha,\mathrm{n})^{16}\mathrm{O}$ in convective regions at higher temperatures (typically $\sim 2.5 \times 10^8$ K).

Various numerical simulations have been proposed to host i-process conditions. These include the proton ingestion during core He flash in very low-metallicity low-mass stars, during the thermal pulse phase of massive AGB (super-AGB) stars of very low metallicity, during the post-AGB phase ("final thermal pulse"), during rapid accretion of H-rich material on white dwarfs, or during shell He-burning in massive very low-metallicity population II or III stars. While the contribution of the i-process to the global galactic enrichment and more particularly to our Solar System remains unclear, it is needed to explain the heavy element patterns observed in peculiar stars, several carbon-enhanced metal-poor (CEMP) stars with simultaneous presence of s-elements and Eu (so-called CEMP-r/s) stars, as well as Sakurai's object V4334 Sgr. More information can be found in Refs. [48–53].

#### 4.1.2.4 The p-Process

The p-process of stellar nucleosynthesis is aimed at explaining the production of the stable neutron-deficient nuclides heavier than iron that are observed in the Solar System and up to now in no other galactic location (for a review see [10]). Various scenarios have been proposed to account for the bulk p-nuclide content of the Solar System, as well as for deviations ("anomalies") with respect to the bulk p-isotope composition of some elements discovered in primitive meteorites. In contrast to the s- and r-processes calling for neutron captures to explain the production of heavy elements, the p-isotopes are produced by photodisintegration reactions on already synthesized s- and r-nuclei. These photoreactions involve ($\gamma$,n), ($\gamma$,p), and ($\gamma$,$\alpha$) reactions at stellar temperatures of the order of 2–3 $\times$ $10^9$ K.

The p-nuclides are mostly produced in the final explosion of a massive star ($M \gtrsim 10\ M_\odot$) as a CCSN or in pre-explosive oxygen-burning episodes [10]. The p-process can develop in the O-Ne layers of the massive stars explosively heated to peak temperatures ranging between 1.7 and 3.3 $\times$ $10^9$ K [54, 55]. The seeds for the p-process are provided by the s-process that develops before the explosion in these stellar mass zones. In this way, as explained above, the O-Ne layers that experience the p-process are initially enriched in $70 \lesssim A \lesssim 90$ s-nuclides.

SNIa have also been suggested as a potential site for the p-process. The p-process nucleosynthesis possibly accompanying the deflagration or delayed detonation regimes has been mainly studied in 1D simulations [56,57] and shown to give rather similar overabundances as CCSN models [10, 58]. However, the predicted SNIa p-nuclide yields suffer from large uncertainties affecting the adopted explosion models as well as the s-seed distributions, detailed information on the composition of the material that is pre-explosively transferred to the white dwarf being missing.

Despite the fact that p-nuclei can be produced consistently with solar ratios over a wide range of nuclei in such scenarios, there remain deficiencies in a few regions, most particularly in the Mo-Ru region where the p-isotopes are strongly underproduced. This fact motivates the search for alternative or additional ways to produce these nuclides. In particular, proton capture and photodisintegration processes in helium star cataclysmics have been suggested as a promising nucleosynthesis source [59]. Such an object is made of a carbon-oxygen white dwarf with sub-Chandrasekhar mass ($M < 1.4 M_\odot$) accumulating a He-rich layer at its surface. An alternative site proposed to explain the origin of the Mo and Ru p-nuclei is the p-rich neutrino-driven wind in CCSNe where antineutrino absorptions in the proton-rich environment produce neutrons that are immediately captured by neutron-deficient nuclei [60].

## 4.2 Nuclear Physics Aspects of Nucleosynthesis

### 4.2.1 Nuclear Reactions of Astrophysical Interest

In a given astrophysical location, two factors dictate the variety of nuclear reactions that can act as energy producers and/or as nucleosynthetic agents. The abundances of the reactants have obviously to be high enough, and the lifetimes of the reactants

against a given nuclear transmutation have to be short enough for this reaction to have time to operate during the evolutionary timescale of the astrophysical site under consideration. The probability of a thermonuclear reaction in an astrophysical plasma is strongly dependent on some specific properties of this plasma. In this respect, two key guiding features are the distribution of the energies of the reacting partners and the reaction cross section at a given energy. First, the reacting nuclei are, locally at least, in a state of thermodynamic equilibrium. In such conditions, all nuclear species obey a Maxwell-Boltzmann distribution of energies, from which it is easily inferred that the relative energies $E_{cm} = \frac{1}{2}\mu v^2$ of the reaction partners also obey such a distribution (where $v$ is the relative velocity between the interacting nuclei 1 and 2 and $\mu = m_1 m_2/(m_1 + m_2)$ their reduced mass). While in laboratory experiments, the target nuclei (T) are typically at rest and the projectiles (P) impinge into the target nuclei at a certain laboratory energy $E_{lab}$, in stellar environments the relative energy is more relevant. Therefore, laboratory experiments should be expressed as a function of the center-of-mass energy $E_{cm} = [M_{\rm T}/(M_{\rm P} + M_{\rm T})] \times E_{lab}$, where $M_P$ and $M_T$ refer to the atomic masses of the projectile and the target (at rest), respectively.

Second, the reaction cross section between charged nuclei is dominated by the probability of penetration of the Coulomb barrier of the interacting nuclei. As a result, the effective reaction rate is obtained by integrating the strongly energy-dependent reaction cross sections over the whole Maxwell-Boltzmann energy range. The resulting integrant exhibits a strong maximum, generally referred to as the Gamow peak. It is centered on the "most effective energy" given by

$$E_0 = 0.1220(Z_1^2 Z_2^2 \mu)^{1/3} T_9^{2/3} \text{ (MeV)} \tag{4.1}$$

where $Z_1$ and $Z_2$ are the proton numbers, $\mu$ the reduced mass (in units of $u$), and $T_9$ the temperature $T$ expressed in GK ($10^9$ K).

The Gamow peak is characterized by a width approximated by

$$\Delta = 4(E_0 k_B T/3)^{1/2} = 0.2368(Z_1^2 Z_2^2 \mu)^{1/6} T_9^{5/6} \text{ (MeV)} \tag{4.2}$$

where $k_B$ is the Boltzmann constant [19].

The reactions thus mostly occur in the approximate window from $E_0 - n\Delta$ to $E_0 + n\Delta$ ($n$ = 2–3), assuming the possible role of resonances is small. For this reason, the energy range of astrophysical relevance for reactions between charged particles is largely above the thermal energy $k_B T$ and much lower than the Coulomb barrier. For these reasons, the sequence of hydrostatic burning episodes is characterized by a limited number of reactions between nuclei with increasing charges, from H-burning to Si-burning, and the charged-particle-induced thermonuclear reactions of relevance concern mainly the capture of protons or $\alpha$-particles which offer the lowest Coulomb barriers. A limited number of fusion reactions involving heavy ions ($^{12}$C, $^{16}$O) are also of great importance.

The considerations above lead to the most effective energy $E_0$ in the case of reactions between charged particles but do not apply to neutron captures in view of

the absence of Coulomb barriers. In this case it can be shown that the most effective energy is of the order of $k_B T$. It has also to be noted that, in contrast to reactions involving charged reactants, the captures of neutrons do not contribute to the energy budget of a star, but are essential players in the synthesis of nuclides heavier than iron through the s-, i-, and r-processes (see Sects. 4.1.2.1–4.1.2.2).

In non-explosive conditions, like in the quiescent phases of stellar evolution which take place at relatively low temperatures, most of the reactions of interest concern stable nuclides. Even so, the experimental determination of their charged-particle-induced cross sections faces enormous problems and represents a real challenge [19]. This relates directly to the smallness of the cross sections due to the fact that $E_0$ lies well below the Coulomb barrier. As a consequence, the cross sections can dive into the nanobarn to picobarn range.

In explosive situations, the temperatures are typically higher than in the non-explosive cases. The corresponding increase of the effective energies $E_0$ gives rise to a higher probability of penetration of the Coulomb barriers and consequently larger cross sections. The price to pay to reach this higher energy domain is huge, however. The nuclear flows indeed depart from the bottom of the valley of nuclear stability and involve more or less unstable nuclei, sometimes all the way very close to the nucleon drip lines (see Fig. 4.3).

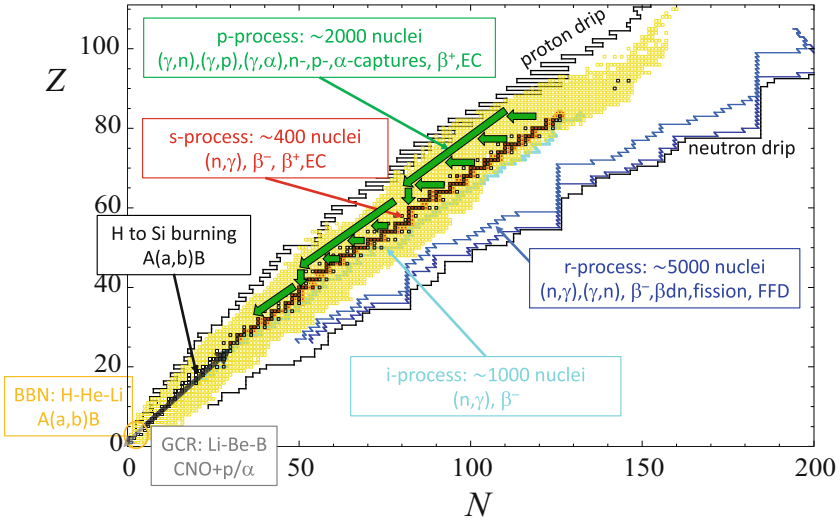


**Fig. 4.3** Schematic representation in the $(N, Z)$ plane of the different nuclear data needs for nucleosynthesis applications. The open black squares correspond to stable or long-lived nuclei, and the open yellow squares to the nuclei with experimentally known masses [21]. Nuclei with a neutron or proton separation energies tending to zero define the neutron or proton "drip lines" (solid black lines), as predicted from a mass model. See text for more details and Ref. [4] (Modified from Ref. [4])

For $\beta$-decays as well as reaction rates, thermally populated nuclear excited states can contribute to the effective stellar rates. The population of the $i^{th}$ excited state with an excitation energy $E_i$ at temperature $T$ can be derived as

$$P_i = \frac{g_i \exp(-E_i/k_B T)}{\sum_i g_i \exp(-E_i/k_B T)}, \tag{4.3}$$

where $g_i = 2J_i + 1$ is the statistical weight and $J_i$ the spin of the state $i$. The denominator is called the partition function $G$. Often a normalized partition function $G^{\text{norm}} = G/g_0 = 1/P_0$ is used to describe the thermal excitations. If $G^{\text{norm}} = 1$, only the ground state is populated ($P_0 = 1$). The thermalization effect is especially noticeable in the case of endothermic reactions on targets with low-lying excited states from which the exit particle channels are greatly favored with respect to the ground state due to restrictions imposed by spin conservation selection rules. The $0^+$ isomeric state at 228 keV in $^{26}$Al is a good example in this respect. It is much shorter-living, with $t_{1/2} = 6.3460(8)$ s, than the $5^+$ ground state with $t_{1/2} = 7.17 \times 10^5$ y. The effective lifetime of $^{26}$Al decreases by many orders of magnitude when moving from 0.2 GK to 1.0 GK due to the thermal excitations populating the isomer [61–64]. In many astrophysical conditions, some isomers may not be thermally populated and act as a separate species with respect to the ground state. The role of astrophysically important isomers has been recently discussed, e.g., in Ref. [65].

In stellar environments, target nuclei at high temperatures have typically no or only a few bound electrons. Instead, they are surrounded by a sea of free electrons. This ionization gives rise to various effects. It has first the obvious effect of reducing the probability of capture of bound electrons but opens the possibility to capture free electrons from the surrounding continuum. A less trivial consequence of ionization relates to the possible development of the process of "bound-state $\beta$-decay," for which the emitted electron is captured in an atomic orbit previously vacated (in part or in total) by ionization. In addition, the reaction rates for charged particle reactions are different from the rates of bare nuclei due to the electron screening. The screening is also present in the laboratory experiments where target nuclei are surrounded by bound atomic electrons. Hence, the measured reaction rates have to be corrected for the electron screening effect to obtain reaction rates between bare nuclei. Finally, in stellar plasmas, a specific electron screening correction has to be applied and can drastically affect the cross sections for bare nuclei [66, 67]. This correction arises because of the ability of a nucleus to polarize its stellar surroundings. As a result, the Coulomb barrier seen by the reacting nuclei is modified in such a way that the tunneling probability, and consequently the reaction rate, increases over its value in vacuum conditions. Different formalisms have been developed depending on the ratio of the Coulomb energy of reacting nuclei to the thermal energy. Weak screening applies if this ratio is well below unity, while a strong screening is obtained when this ratio is well in excess of unity. In this case, a very large increase of the reaction rates is predicted. The limiting situation of strong screening is reached when solidification of the stellar plasma leads to the

special pycnonuclear regime [66, 67]. In this case, the reactions are not governed by temperature like in the thermonuclear regime, but instead by lattice vibrations in dense Coulomb solids. This limiting regime can be approached e.g. at the high densities and low temperatures prevailing in white dwarfs.

### 4.2.2 Data Needed for the Various Nucleosynthesis Processes

Strong, weak, and electromagnetic interaction processes play an essential role in nuclear astrophysics. As shown in Fig. 4.3, a very large amount of nuclear information is necessary in order to model the various nucleosynthesis processes. These concern the decay properties of a large variety of light to heavy nuclei between the proton and neutron drip lines, including the $\beta$-decay or electron capture rates as well as $\alpha$-decay or spontaneous fission probabilities for the heavy species. For the nuclei lighter than iron, most of the reactions involved during the BBN or the H- to Si-burning stages concern the capture of protons and $\alpha$-particles at relatively low energies (far below 1 MeV for neutrons and the Coulomb barrier for charged particles). A limited number of fusion reactions involving heavy ions ($^{12}$C, $^{16}$O) are also of direct impact during C and O-burning phases. The nuclear data needed to explain the Li-Be-B nucleosynthesis is quite different since it mainly involves spallation reactions between CNO nuclei accelerated at high energies interacting with the interstellar H and He. A review of the relevant reactions and the precision at which they are needed can be found in Ref. [68].

In addition to reaction rates, some nuclear structure properties, in particular the nuclear mass, may play a key role in nucleosynthesis applications. More specifically, if the r-process nucleosynthesis takes place at sufficiently high temperatures $T$ and high neutron densities $N_n$, the neutron captures and their inverse photodisintegrations become much faster than $\beta^-$ decays [69]. In this case, a $(n,\gamma) \rightleftarrows (\gamma,n)$ equilibrium may be established, and the abundances within each isotopic chain determined by the Saha equation (see, e.g., Ref. [10]):

$$\frac{N(A+1,Z)}{N(A,Z)} = N_n \left(\frac{h^2}{2\pi\mu k_B T}\right)^{3/2} \frac{2J(A+1,Z)+1}{(2J(A,Z)+1)(2J_n+1)} \times \frac{G^{\mathrm{norm}}(A+1,Z)}{G^{\mathrm{norm}}(A,Z)} e^{Q_{n,\gamma}/(k_B T)}, \tag{4.4}$$

where $Q_{n,\gamma} = [m(A,Z) + m_n - m(A+1,Z)]\,c^2$ is the $Q$-value for a neutron capture on nucleus $(A,Z)$ or, in other words, the neutron separation energy $S_n$ of the nucleus $(A+1,Z)$, $Q_{n,\gamma}(A,Z) = S_n(A+1,Z)$. Equation 4.4 highlights the importance of nuclear masses in defining the r-process path at a given time. In NS merger models, the r-process may take place at relatively low temperatures [39], and, at some point, the neutron captures will freeze out, so that the $(n,\gamma) \rightleftarrows (\gamma,n)$ equilibrium is not expected to be established all along the irradiation time. In this case, the abundances cannot be determined simply using Eq. 4.4 but become

sensitive to the neutron capture and photoneutron reaction rates. Nuclear masses remain, however, key in estimating the competition between neutron captures, photoneutron emissions, and $\beta$-decays.

Fission may also play an important role during the r-process nucleosynthesis though the exact role played by fission on r-abundance distribution strongly depends on the hydrodynamic modeling of the initial neutron richness found in the astrophysical plasma. In astrophysical sites characterized by a large initial neutron richness, e.g., in NS-BH mergers, fission may play a fundamental role, more particularly by (*i*) recycling the matter during the neutron irradiation (or if not, by allowing the possible production of superheavy long-lived nuclei, if any); (*ii*) shaping the r-abundance distribution in the $110 \leq A \leq 170$ mass region at the end of the neutron irradiation; (*iii*) defining the residual production of some specific heavy stable nuclei, more specifically Pb and Bi, but also the long-lived cosmochronometers Th and U; and (*iv*) heating the environment through the energy released [40, 70–72]. In addition to spontaneous fission, neutron-induced and $\beta$-delayed fission processes are important for the r-process. In the neutron-induced fission, the additional energy required to overcome the fission barrier is provided by neutrons. In the $\beta$-delayed fission mode, the $\beta$-decay may lead to an excited state with an excitation energy $E_x$ close to the fission barrier height $B_f$ in the daughter nucleus.

Although important effort has been devoted in the last decades to measure reaction cross sections or nuclear structure properties of astrophysical interest (see Sect. 4.3), experimental data only covers a minute fraction of the whole set of data required for nucleosynthesis applications. Reactions of interest often concern unstable or even exotic (neutron-rich, neutron-deficient, superheavy) species for which no experimental data exist. Given applications (in particular, the nucleosynthesis of elements heavier than iron) involve a large number (thousands) of unstable nuclei for which many different properties have to be determined. Finally, the energy range for which experimental data is available is restricted to the small range reachable by present experimental setups. To fill the gaps, only theoretical predictions can be used, as discussed in Sect. 4.4.

## 4.3 Nuclear Astrophysics with Radioactive Beams

In order to model various nucleosynthesis processes (see Sect. 4.1.2), different types of nuclear data are needed as discussed in Sect. 4.2.2. For lighter nuclei, the key reactions concern proton and alpha captures. For quiescent hydrogen and helium burning, the relevant temperatures are on the order of 10–100 MK, corresponding to center-of-mass energies less than (or around) 100 keV, far below the Coulomb barriers. As a result, the reaction cross sections for the relevant proton and alpha captures are very low. This poses several challenges. Typically the experiments have not yet reached the relevant energy region but provide cross sections at higher energies, requiring extrapolations down to the relevant energies. Natural background is a major limiting factor for the experiments. Therefore, many direct measurements

for stellar burning are nowadays carried out in underground laboratories or other low-background locations. A recent review [73] summarizes the status of these experiments. Here we focus on experiments employing radioactive beams for nuclear astrophysics. Free neutrons are radioactive with a half-life of around 10 mins, but we will not discuss experiments involving neutron beams, which are very important, for example, for the s-process. The status of experiments utilizing neutron beams for astrophysics has been reviewed, for example, in Refs. [73, 74].

### 4.3.1 Nuclear Reactions in Inverse Kinematics with Radioactive Beams

Many reactions on radioactive nuclei are usually easier to study in inverse kinematics with a radioactive beam on a stable target. As an example, proton-capture reactions can be studied with a radioactive beam on a hydrogen target instead of using normal kinematics, i.e., a proton beam on a radioactive target. For shorter-lived nuclei, inverse kinematics is the only option available. The same applies to other reactions involving radioactive nuclei.

Let us consider the reaction $^{26}$Al$(p, \gamma)^{27}$Si as an example. This reaction is relevant for the abundance of the cosmic $\gamma$-ray emitter $^{26}$Al and the observation of its 1809-keV $\gamma$-rays with space-based telescopes, such as INTEGRAL [75]. Due to the relatively long half-life of $^{26}$Al, $t_{1/2} = 7.17 \times 10^5$ y, a study in normal kinematics is also feasible. The reaction was investigated using proton beams with laboratory energies from 170 keV to 1.5 MeV in the 1980s [76]. Later, it was revisited using the DRAGON recoil separator at TRIUMF and employing a radioactive $^{26}$Al beam with laboratory energies of 5.226 MeV and 5.122 MeV [77]. There, $^{26}$Al was produced with a 70-$\mu$A proton beam on a SiC target.

Radioactive beams for inverse kinematics studies can be produced via nuclear reactions, such as fusion evaporation, fragmentation, or fission, but specific beams can be created using long-lived isotopes extracted from radioactive waste [78]. For example, $^{44}$Ti ($T_{1/2} = 85$ y) was extracted from the copper beam dump used for the 590-MeV protons at the Paul Scherrer Institute and later utilized in an experiment at ISOLDE (CERN) [79]. Beam intensities up to around $2 \times 10^6$ particles per second were delivered and accelerated to 2.1 MeV/u at REX-ISOLDE before impinging into a helium target [79]. The experiment provided an upper limit estimate for the $^{44}$Ti$(\alpha, p)^{47}$V reaction cross section within the Gamow window. The limit is at least a factor of 2.2(13) lower than given by the Hauser-Feshbach calculation with the NON-SMOKER reaction code. This brings the calculated $^{44}$Ti abundances closer to the observations of the $^{44}$Ti yields in Cas A [80, 81] and SN1987A [82] supernova explosions.

Studies of proton captures on light- or intermediate-mass nuclei usually focus on the determination of resonance strengths $\omega\gamma$ because the total reaction rate is typically dominated by a few resonances. The resonance strength for a proton-capture reaction on a target nucleus with spin $J_T$, leading to a resonant state with

spin $J_{\mathrm{res}}$, is determined as

$$\omega\gamma = \frac{(2J_{\mathrm{res}}+1)}{(2J_p+1)(2J_T+1)}\frac{\Gamma_p\Gamma_\gamma}{\Gamma_p+\Gamma_\gamma}\,, \tag{4.5}$$

where $J_p$ is the proton spin (1/2) and the $\Gamma_p$ and $\Gamma_\gamma$ are the proton and gamma partial widths for the resonance, respectively. From Eq. 4.5, it is clear that at low resonance energies, where the probability for the proton emission is still low ($\Gamma_p \ll \Gamma_\gamma$), the resonance strength is almost entirely determined by the proton width $\Gamma_p$. It can be written as $\Gamma_p = C^2S\ \Gamma_{p,sp}$, where $C^2S$ is the spectroscopic factor of the state and $\Gamma_{p,sp}$ the single-particle proton width obtained, e.g., via shell-model calculations.

Estimates on relevant spectroscopic factors can be obtained using surrogate methods. Instead of proton captures, the relevant states can be explored via $(d,n)$ proton-transfer reactions. Recently, many studies on this topic have been carried out at the National Superconducting Cyclotron Laboratory. For example, the $^{26}$Al$(p,\gamma)^{27}$Si reaction was studied using a 30 MeV/u $^{26}$Al$^{13+}$ beam on a deuterated polyethylene, $(CD_2)_n$ target. Spectroscopic factors for states close to the proton threshold in $^{27}$Si were obtained by comparing the experimentally determined cross sections to the theoretical predictions for the reaction $^{26}$Al$(d,n)^{27}$Si [83]. The results were in agreement with a previous ($^3$He, $d$) study [84], supporting the feasibility of the method. The surrogate technique using $(d,n)$ proton-transfer reactions has been applied to the bottleneck reaction in the nova nucleosynthesis, $^{30}$P$(p,\gamma)$ [85], and for the key reaction to bypass the waiting-point nucleus $^{56}$Ni in type I X-ray bursts, $^{56}$Ni$(p,\gamma)^{57}$Cu [86].

In addition to $(d,n)$ reactions, relevant information on the resonance states in explosive hydrogen burning scenarios, such as novae and type I X-ray bursts, is obtained via many other methods. $\beta$-delayed proton and gamma emissions provide data on the gamma and proton widths of the resonance states. However, $\beta$-decay selection rules limit the resonant states that are populated. For example, $\beta$-decay of $^{31}$Cl populates excited states in $^{31}$S that further de-excite via gamma and proton emissions. Thus, the resonant states in the reaction $^{30}$P$(p,\gamma)^{31}$S can be studied inversely via $\beta$-decay. The $\beta$-decay studies have, e.g., indicated a strong $3/2^+$ resonance at 6390 keV in $^{31}$S [87]. Information on the excitation energies, spins, and parities of the resonance states is also obtained via high precision gamma spectroscopy and transfer-reaction studies, e.g., employing ($^3$He, $t$) reactions. These studies are not limited by such selection rules like $\beta$-decay experiments and therefore cover a larger set of states.

### 4.3.2 Properties of Exotic Nuclei with Radioactive Beams

Many astrophysical processes proceed via exotic radioactive nuclei as discussed in Sect. 4.1.2. Progress in radioactive beam facilities and measurement techniques has opened new possibilities to study, e.g., nuclei relevant for the r- and i-processes

traversing through neutron-rich nuclei. For the r-process, many nuclei will remain experimentally inaccessible and require solid nuclear models (see Sect. 4.4). Experimental data are, however, essential for testing the existing nuclear models and their applicability in different regions of the nuclear chart. The following subsections give a brief overview on experimental techniques and recent experimental results on nuclear properties relevant for nuclear astrophysics, in particular for the r-process.

#### 4.3.2.1 Masses of Exotic Nuclides and Related Techniques

Nuclear masses play a key role in the modeling of astrophysical processes. The reaction $Q$ value, i.e., the energy required for, or released in a reaction, is determined by nuclear masses, $Q = \left(\sum_i m_i - \sum_f m_f\right) c^2$, where $m_i$ and $m_f$ are the mass values for the initial and final states of a reaction. The $Q$ values have a strong effect on reaction and decay rates and therefore have to be known rather precisely for accurate nuclear reaction network calculations.

In practice, experiments determine atomic masses $M(A, Z) = m(A, Z) + Zm_e - B_e(A, Z)/c^2$, where $B_e(A, Z)$ is the total electron binding energy for an atom with mass number $A$, proton number $Z$, and nuclear mass $m(A, Z)$. The effect of electron binding energy is usually small though it may contribute, e.g., for low-energy resonant captures involving fully stripped atoms in stellar plasma [88]. As the proton number conserves in nuclear reactions, the electron masses cancel out in the estimate of the $Q$ value. Only for $\beta^+$ decays, the electron masses need to be taken into account in the $Q$-value calculation.

#### 4.3.2.2 Penning-Trap Mass Spectrometry

Several mass measurement methods are used to determine masses of radioactive nuclei. Penning-trap mass spectrometry is the most precise technique at the moment. In a Penning trap, ions are confined radially by a strong, homogeneous magnetic field $B$ and axially by a quadrupolar electric field. The ions have three eigenmotions, axial motion with a frequency $\nu_z$ and two radial motions with the reduced cyclotron $\nu_+$ and magnetron $\nu_-$ frequencies. For an ion with charge $q$ and mass $m$ in an ideal Penning trap, the two radial motions sum up to the cyclotron frequency $\nu_c$:

$$\nu_c = \nu_+ + \nu_- = \frac{1}{2\pi}\frac{q}{m}B \tag{4.6}$$

In reality, there are misalignments, e.g., in the magnetic field axis or imperfections in the quadrupolar electric field. The invariance theorem [89,90] holds even for these more realistic conditions, coupling the three eigenmotions together:

$$\nu_c^2 = \nu_+^2 + \nu_-^2 + \nu_z^2. \tag{4.7}$$

Traditionally, Penning traps have utilized the time-of-flight ion cyclotron resonance (ToF-ICR) method [91,92] to determine ion's cyclotron resonance frequency. In this method, the ions are excited using a quadrupolar radiofrequency pulse with

a frequency $\nu_{RF}$ and a specific amplitude and duration. The $\nu_{RF}$ is scanned around the expected $\nu_c$. When $\nu_{RF} = \nu_c$, the ions are in resonance and gain most energy. This results in the shortest time of flight when the ions are extracted from the trap through a strong magnetic field gradient to an ion detector, typically a microchannel-plate (MCP) detector. The magnetic field strength $B$ is determined by performing a similar measurement with a reference ion which has a well-known mass in literature. The ToF-ICR method takes a rather long time as several frequency points have to be measured around the cyclotron resonance frequency in order to fit the resonance curve to the data. An example of a TOF-ICR spectrum is given in the bottom panel of Fig. 4.4. The quadrupolar excitation times range from around 50 ms up to around 1600 ms, and the total measurement cycle typically takes ≈400–1200 ms. Therefore, the Penning-trap mass spectrometry is often limited to nuclei with half-lives longer than ≈100 ms. However, in specific cases, where the production rates are high enough, measurements of shorter-living nuclides can also be done with the ToF-ICR method.

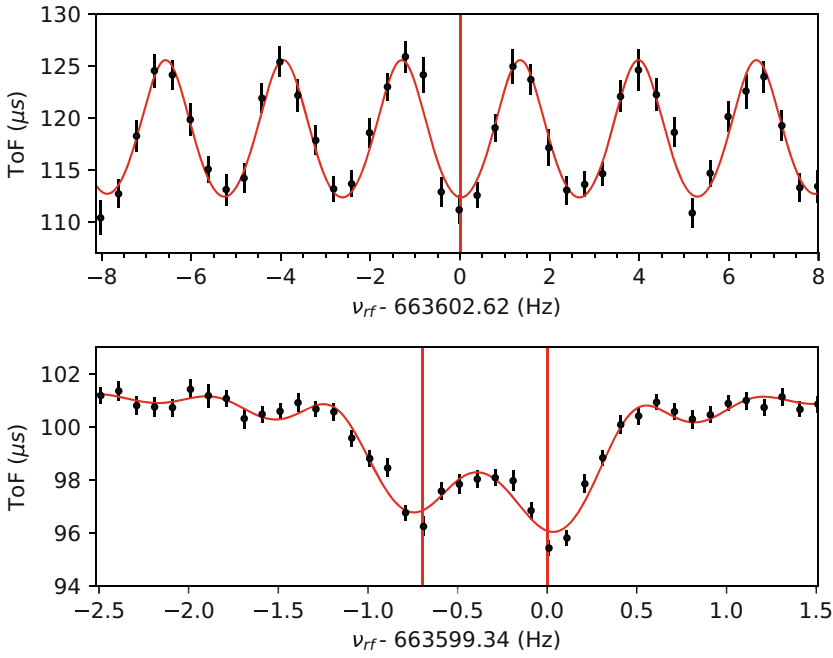


**Fig. 4.4** Examples of ToF spectra measured for $^{162}Eu^{+}$ ions using a 25-350-25ms (on-off-on) excitation pattern (top) and 1600-ms continuous quadrupolar excitation. The shorter excitation time (top panel) was not sufficient to resolve the low-lying isomeric state from the ground state. In the bottom panel, the cyclotron resonance frequency for the ground state is located at the minimum time of flight indicated with a vertical line at zero. The isomeric state is located at a lower frequency, indicated by the other vertical line. The red curve is a fit to the theoretical lineshape. The fit requires several measured data points (shown in black) around the cyclotron frequency (Reprinted from Ref. [95] with permissions from the American Physical Society)

A slightly higher precision is achieved with the so-called Ramsey method [93, 94], where instead of a continuous quadrupole excitation, time-separated oscillatory fields are applied. In other words, two excitation pulses, each with a rectangular envelope, are applied with a certain time in between when the excitation is off. An example of a Ramsey type of a resonance is given in the upper panel of Fig. 4.4. There, $^{162}Eu^{+}$ ions have been studied using a 25-350-25ms (on-off-on) excitation pattern (see the top panel of Fig. 4.4). It yields a better precision compared to a 400-ms continuous quadrupolar excitation; however, the resolving power is still not sufficient to resolve the low-lying isomeric state from the ground state. This is achieved with a 1600-ms quadrupolar excitation shown in the bottom panel of Fig. 4.4. It also illustrates how the resolving power of a Penning trap is proportional to the excitation time. The longer the excitation time, the better the resolving power.

The phase-imaging ion cyclotron resonance (PI-ICR) method [96, 97] provides around 40 times better resolving power than the ToF-ICR method. The method is superior in resolving low-lying isomeric states from the ground states, often useful for accurate mass measurements. The frequencies $\nu_{\pm}$ for the radial ion motions are obtained from the phase $\phi_{\pm}$ the ion accumulates after time $t$:$\nu_{\pm} = \frac{\phi_{\pm}+2\pi n}{2\pi t}$, where $n$ is the number of full revolutions ion does during the time $t$. The phase is determined using a position-sensitive MCP detector. Finally, the cyclotron frequency is computed as a sum of the two radial frequencies (see Eq.4.6), and the mass is derived from the frequency ratio similar to the ToF-ICR method. The benefit of the PI-ICR method is that every ion counts, i.e., instead of scanning a broad range of frequencies around the cyclotron frequency, every measured ion adds to the phase spot in the 2D image of the ion motion. Figure 4.5 shows an example of a PI-ICR measurement. The PI-ICR method is also applicable to cases with low yields, such as superheavy nuclides [98]. In addition to the ToF-ICR and PI-ICR, Fourier-transform ion cyclotron resonance (FT-ICR) method [99] can be applied in Penning traps; however, it has not yet been widely used for studies of radioactive nuclides due to its complexity. For a recent review on Penning-trap measurements, see, e.g., Refs. [100, 101].

#### 4.3.2.3 Multi-Reflection Time-of-Flight Mass Spectrometers

Multi-reflection time-of-flight (MR-ToF) [102] mass spectrometers offer a faster way to determine masses of exotic nuclides than Penning traps. The method also saves measurement time as several nuclides can be measured at once. The ions injected into a MR-ToF are typically prepared in a radiofrequency quadrupole cooler and buncher at a potential $V$. They gain a kinetic energy $E_{kin.} = qV = mv^2/2$, where $v$ is the velocity of the ions. As a result, for the same flight path, the flight time $t$ is inversely proportional to the ion's velocity, $t \propto 1/v \propto \sqrt{(m/q)}$, and can be determined as

$$t = a\sqrt{\frac{m}{q}} + b, \tag{4.8}$$

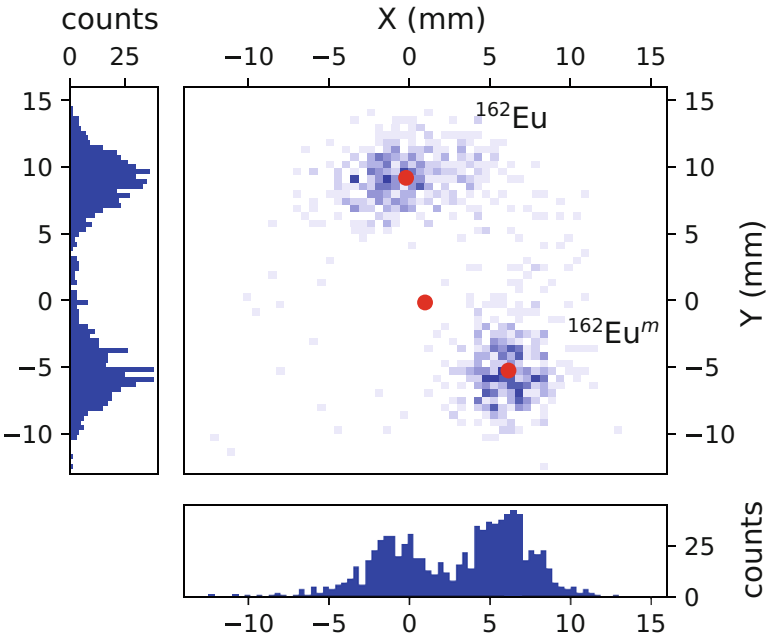


**Fig. 4.5** An example of a PI-ICR measurement of $^{162}Eu^{+}$ ions. The image of the cyclotron motion of $^{162}Eu^{+}$ is magnified and projected onto a position-sensitive detector located outside the Penning trap. The two detected ion spots correspond to the ground and isomeric state of $^{162}$Eu. The blue squares show the total number of ions in each bin, darker shading indicating more ions. The red dots show the centers of the cyclotron motion images of the ground and isomeric states and the center of the precision trap. The number of ions projected on the x and y axes is also shown. Positions can be fitted even with a moderate statistics because every ion contributes to the determinations of the spot positions from which the phases, and eventually the cyclotron frequency ratios are determined (Reprinted from Ref. [95] with permissions from the American Physical Society)

where $a$ and $b$ are device-specific parameters. The achieved precision is typically somewhat lower than in Penning-trap mass spectrometry, and the resolving power is not sufficient to resolve low-lying isomeric states (E $\lesssim$100 keV). Due to the simple and cost-effective solution for fast and precise mass measurements, MR-ToF mass spectrometers are nowadays widely used in accelerator laboratories around the world. MR-ToF mass spectrometers, e.g., at ISOLDE/CERN [103], at the FRS Ion Catcher in GSI/FAIR [104, 105], and at the TITAN facility in TRIUMF [106], have been utilized for nuclear astrophysics studies. An example of a MR-ToF measurement is shown in Fig. 4.6.

#### 4.3.2.4 Storage Rings

Storage rings have been used for mass measurement of exotic ions for three decades [108]. There are two techniques utilized for mass measurements in storage rings,

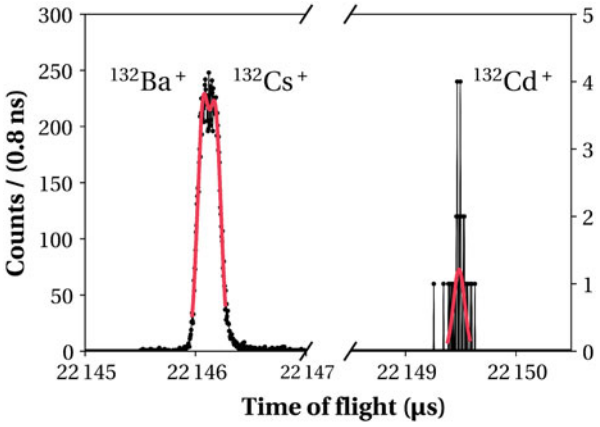


**Fig. 4.6** An example of a MR-ToF measurement of $^{132}$Cd at ISOLTRAP. Time-of-flight spectrum after 800 revolutions shows the $^{132}Cd^+$ peak along with isobaric ions ($^{132}Ba^+$ and $^{132}Cs^+$), used for the calibration together with $^{133}Cs^+$. Gaussian fits (in red) are also shown. MR-ToF method is suitable for measurements with low statistics (Reprinted from Ref. [107])

but both methods determine the ion's revolution frequency $f$ in the ring:

$$\frac{\delta f}{f} = -\frac{1}{\gamma_t^2}\frac{\delta(m/q)}{(m/q)} + \left(1 - \frac{\gamma^2}{\gamma_t^2}\right)\frac{\delta v}{v}, \tag{4.9}$$

where $\gamma = 1/\sqrt{1-(v/c)^2}$ is the Lorenz factor and $\gamma_t$ is an ion-optical parameter of the storage ring known as the transition energy. In practice, usually revolution times are measured and plotted instead of the revolution frequency.

In the Schottky method, the ions are cooled with electrons to minimize the velocity spread $\delta v$. This takes several seconds and limits the use of the Schottky method for shorter-lived nuclei. In the isochronous mass spectrometry (IMS) method, the ions of interest are injected with energies corresponding to $\gamma = \gamma_t$, and no additional cooling is required. The benefit in the IMS method is that a broad variety of ions can be simultaneously measured, and the method is much faster than, e.g., Penning-trap mass spectrometry. An example of an isochronous mass measurement is shown in Fig. 4.7. There are three main storage ring facilities for mass measurements at the moment: Experimental Storage Ring (ESR) [109] at GSI/FAIR, CSRe [110] in Lanzhou and R3 [111] at BigRIPS in RIKEN. Storage rings can also be utilized for reaction cross-sectional measurements for nuclear astrophysics, as exemplified for the $^{96}$Ru$(p,\gamma)$ [112] and $^{124}$Xe$(p,\gamma)$ [113] reactions at the ESR ring.

#### 4.3.2.5 Time of Flight and Magnetic Rigidity

For the most exotic and shortest-lived nuclei, masses can be determined at fragment separator facilities utilizing the relationship between the time of flight and magnetic

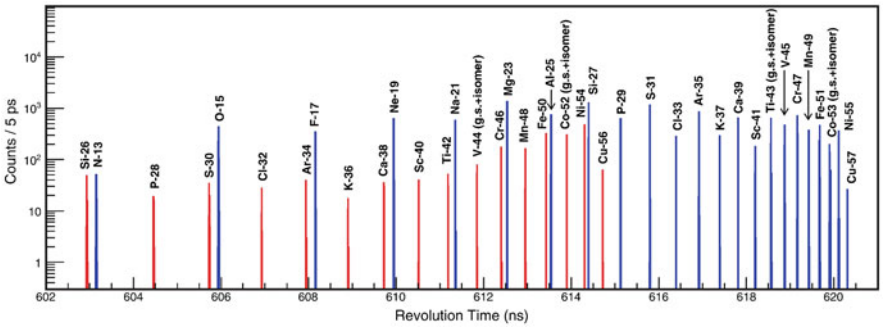


**Fig. 4.7** An example of a revolution time spectrum from a storage ring measurement on proton-rich nuclei using isochronous mode at CSRe. The red and blue peaks represent the $T_Z = (N - Z)/2 = -1$ and $T_Z = -1/2$ nuclei, respectively (Reprinted from Ref. [114] with permissions from the American Physical Society)

rigidity $B\rho$:

$$(m/q) = \frac{t}{L}\frac{B\rho}{\gamma}, \tag{4.10}$$

where $t$ is the time of flight and $L$ is the length of the flight path. The dependence of $m/q$ on the time of flight can be calibrated using a set of ions with a well-known mass. The ToF-$B\rho$ technique can only provide a modest precision of several hundreds of keV, but it can be applied also to very short-lived nuclei ($t_{1/2} < \mu$s). Although the lack of precision hinders detailed studies of nuclear structure, general trends and large changes on the mass surface can be detected with the ToF-$B\rho$ method as demonstrated, e.g., in Refs. [115–118].

#### 4.3.2.6 Current Status and Recent Mass Measurements for Nuclear Astrophysics

Table 4.1 summarizes typical precisions achieved for mass-excess values $\Delta = (M(A, Z) - A \cdot u)c^2$ (where $u$ is the atomic mass unit) using different mass measurement techniques and rough half-life limitations or ranges for the experiments. Experimental atomic mass values are evaluated regularly in the so-called atomic mass evaluations (AME). The evaluation takes into account available experimental mass data from various experiments. Experiments provide mass values with respect to other nuclides, e.g., Penning-trap measurements are done with respect to a reference nuclide, and reaction $Q$-values connect the reactants and products. The AME takes into account all the connections between nuclei and does a least squares optimization of the data, weighted by the experimental uncertainties $\sigma_{\mathrm{exp},i}$ as $w_i = 1/\sigma^2_{\mathrm{exp},i}$ [119]. The optimization yields adjusted mass values tabulated in the AME mass tables. The AME also reveals irregular or anomalous experimental data points deviating from the otherwise smooth mass surface. The most recent

**Table 4.1** Different mass measurement techniques, typical precisions achieved for the mass-excess values, and half-life limitations. The precision and half-life limits depend on several factors, such as the production rates and measurement times (statistics). The values are mainly to give an idea of the strengths and weaknesses of the methods

| Method | Precisions | Half-lives |
|---|---|---|
| ToF-ICR | ∼0.5–50 keV | $\gtrsim$100 ms |
| PI-ICR | ∼0.5–20 keV | $\gtrsim$50 ms |
| MR-TOF | ∼20–150 keV | $\gtrsim$10 ms |
| Schottky MS | ∼1–50 keV | $\gtrsim$1 s (cooling) |
| Isochronous MS | ∼10–200 keV | $\gtrsim$10 μs |
| ToF-B$\rho$ | ∼300–500 keV | $\gtrsim$ below 1 μs |

AME is AME2020 [21]. The NUBASE evaluations on the ground and isomeric state properties are published together with the AME, with the most recent being NUBASE2020 [120].

Many mass measurements for nuclear astrophysics have been performed recently. For example, masses of 22 neutron-rich rare-earth nuclei have been studied with the JYFLTRAP Penning trap [121], 14 for the first time [95, 122]. The measurements indicated less odd-even staggering in the neutron separation energies than predicted by the commonly used mass models for the r-process calculations (see Sect. 4.4.1). Including the new mass values in the *r*-process calculations resulted in a smoother trend in the calculated r-process abundances.

The recent precision mass measurements of neutron-rich $^{126-132}$Cd isotopes [107, 123] using the ISOLTRAP Penning trap [107] and its MR-ToF mass spectrometer [103] have reduced the nuclear uncertainties around the second r-process abundance peak. Mass measurements with the MR-ToF mass spectrometer at TITAN [106, 124] and the JYFLTRAP Penning trap [125] have provided new mass data for the first r-process peak region.

#### 4.3.2.7 $\beta$-Decay Experiments for Nuclear Astrophysics

$\beta$-Decay plays an essential role in neutron-capture processes. The conversion to heavier elements is almost solely done via $\beta^-$ decays, which compete with neutron captures (and photodisintegrations for high-temperatures environment). As a result, the $\beta$-decay half-lives serve as an important input in the nucleosynthesis calculations.

For the r-process, dozens of $\beta$-decay half-lives have been recently determined employing fragmentation or in-flight fission of $^{238}$U at GSI and at Radioactive Isotope Beam Factory (RIBF) at RIKEN [126–130]. For given magnetic rigidity $B\rho = mv/q$, the fragments are identified based on (i) their energy loss $\Delta E$ and (ii) time of flight through the fragment separator. The energy loss is proportional to the proton number $Z^2$, i.e., heavier elements leave more energy. The energy loss is typically determined using an ionization chamber or stacked silicon detector. The time of flight is usually determined between two scintillator detectors and

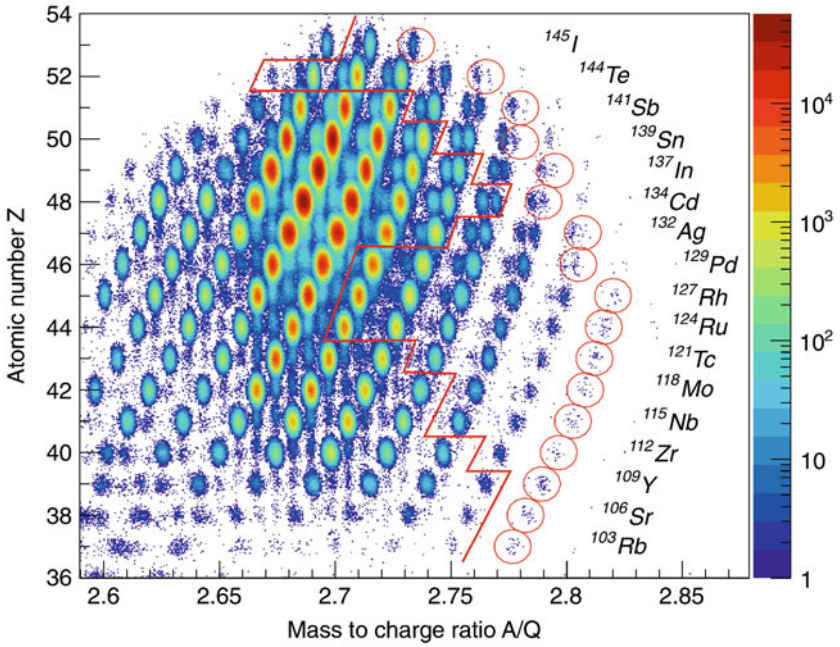


**Fig. 4.8** An example of a particle identification (PID) plot. Ions are identified based on their proton number $Z$ and the mass-to-charge ratio. The heaviest studied isotopes are labeled and highlighted by a red circle (Reprinted from Ref. [127] with permissions from the American Physical Society)

is proportional to $m/q$. A particle identification (PID) plot (see Fig. 4.8 for an example) typically shows the energy loss versus the time of flight but calibrated to show the proton number $Z$ versus $A/q$.

$\beta$-decay half-lives at fragment separator facilities are usually determined by implanting the beam into a stack of silicon detectors and measuring the time difference between the implantation and $\beta^-$ particles (electrons). During the last decade, the knowledge of the half-lives of neutron-rich nuclei has increased substantially. The measurements at GSI and RIBF have provided around 240 half-life values: around 20 half-lives close to $^{78}$Ni [126], 94 in the rare-earth region [130], 110 in the $N = 82$ region [127], and 20 new half-lives in the $N = 126$ region [128, 129]. An example of a $\beta$-decay half-life measurement is shown in Fig. 4.9.

$\beta$-decays can be studied also at isotope separator on-line (ISOL) facilities, but there the selection of the isotope happens already before the beam arrives at the detector setup. As a result, the experiments focus on one or a few isotopes during a beamtime. On the other hand, $\beta$-decay studies at ISOL facilities can be done with very pure beams (see Fig. 4.10). Even isomerically pure beams can be prepared, e.g., by using a Penning trap or selective laser ionization.

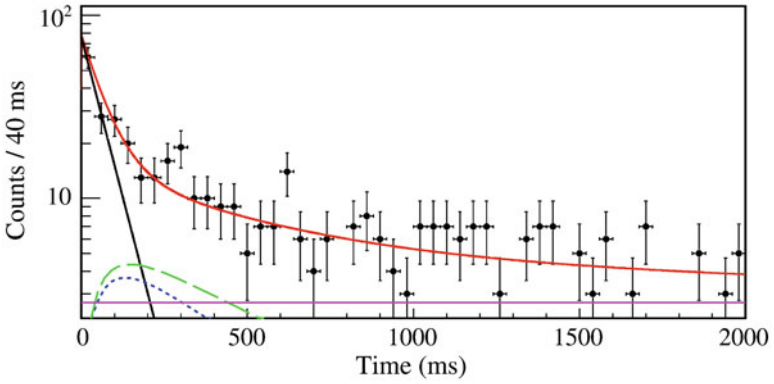


**Fig. 4.9** Half-life measurement of $^{79}$Ni at RIBF. Time distribution of the $\beta$-decay events correlated with the implanted $^{79}$Ni ions has been plotted. The fitting function (solid red line) considers the activities of parent nuclei (dashed-dotted black line), $\beta$-decay daughter nuclei (fine-dashed blue line), $\beta n$-decay daughter nuclei (dashed green line), and a constant background (solid pink line). A half-life of $43.0^{+8.6}_{-7.5}$ ms was determined for $^{79}$Ni (Reprinted from Ref. [126] with permissions from the American Physical Society)

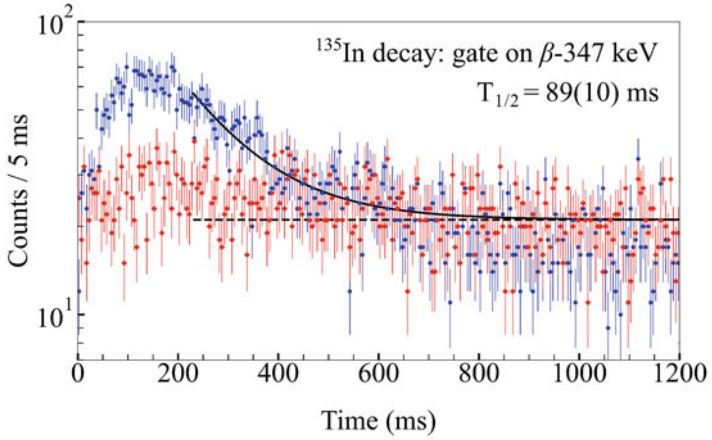


**Fig. 4.10** Half-life measurement of $^{135}$In at the ISOLDE Decay Station, where the laser-ionized $^{135}In^+$ beam was accelerated to 40 keV and implanted into an aluminized Mylar tape at the center of the detection setup. The time distribution relative to the proton pulse from the CERN Proton Synchrotron Booster is shown as blue data points for the $\beta$-gated 347-keV $\gamma$-ray transitions, which belong to the $\beta$-delayed neutron daughter $^{134}$Sn. The radioactive beam was extracted for period 5–230 ms, followed by the decay. The red data points represent the background (Reprinted from Ref. [131])

$\beta$-decays are also essential during the freeze-out phase of the r-process when matter is decaying back to stability. Prior to the freeze-out, the abundance pattern has an odd-even effect due to the odd-even staggering of neutron separation energies. Even-$N$ nuclei are more abundant than their neighboring odd-$N$ nuclei in each

isotopic chain. This can also be seen in Eq. 4.4, where $Q_{n,\gamma}$ is higher for a nucleus $(A, Z)$ with an odd neutron number $N$. During the freeze-out, $\beta$-delayed neutron emissions smoothen the abundance pattern.

In $\beta$-delayed neutron emission, $\beta$-decay of a nucleus $(A, Z)$ will lead to an excited state above the neutron separation energy $S_n(A, Z + 1)$ in the daughter nucleus $(A, Z + 1)$. Since the state is neutron-unbound, it will emit a neutron and lead to a nucleus $(A - 1, Z + 1)$. $\beta$-delayed neutron emission ($\beta n$) was discovered already in 1939 [132]. Later, also $\beta$-delayed two-neutron ($\beta 2n$) [133], three-neutron ($\beta 3n$) [134], and four neutron ($\beta 4n$) [135] decays have been discovered, leading to nuclei $(A - 2, Z + 1)$, $(A - 3, Z + 1)$, and $(A - 4, Z + 1)$, respectively. For the r-process calculations, the $\beta$-delayed neutron emission branching ratios are relevant to determine the flow from one mass number to another.

$\beta$-delayed neutron branching ratio measurements are nowadays based on $^3$He counters located in a neutron energy moderator medium, such as polyethylene. The detection of neutrons is based on the reaction $^3\mathrm{He}(n, p)^3\mathrm{H}$, which releases 764 keV of energy. This is easily detectable and clearly above the noise level. Neutrons are moderated because the cross section for the used detection reaction increases with decreasing neutron energy. The BEta-deLayEd Neutron (BELEN) counter [136] has been designed for the FAIR DESPEC experiment. It has already been utilized in experiments at the ion guide isotope separator on-line (IGISOL) facility [137], where the JYFLTRAP Penning trap was used to select the ions of interest for the $\beta$-decay studies. For example, $\beta$-delayed two-neutron emission from $^{136}$Sb has been studied at IGISOL [138]. More recently, a massive campaign of $\beta$-delayed neutron emission measurements has been performed with the BRIKEN (Beta-delayed Neutron Measurements at RIKEN) [139] setup at RIBF. The BRIKEN collaboration has already measured neutron emission probabilities for more than 180 nuclei. In addition to $\beta$-delayed neutron emission probabilities, $\beta$-delayed neutrons provide a way to determine $\beta$-decay half-lives. A recent compilation on $\beta$-delayed neutron emission summarizes the current status [140].

#### 4.3.2.8 Neutron-Capture Rates

Neutron-capture rates on radioactive short-lived nuclei are challenging to study. However, many factors affecting the neutron-capture rate calculations can be investigated at radioactive beam facilities. Mass measurements provide data on neutron-capture $Q$ values. The $\beta$-Oslo method [141, 142] yields information on level densities and $\gamma$-ray strength functions for moderately neutron-rich nuclei. The technique utilizes segmented total absorption $\gamma$-ray spectrometers with which both the individual $\gamma$-rays and the $\gamma$-ray cascade, i.e., the excitation energy, can be determined. In order to efficiently use this method, the $\beta$-decay $Q$ value has to be high enough but the neutron-separation energies not too low. This maximizes the range of states that can be detected via $\beta$-delayed gamma cascades.

For specific cases, neutron-transfer $(d, p)$ reactions provide information on the key resonance states and spectroscopic factors. For example, single-particle states in $^{133}$Sn isotopes have been studied using the $^{132}\mathrm{Sn}(d, p)^{133}\mathrm{Sn}$ reaction in inverse kinematics [143]. The method has similarities with the $(d, n)$ reactions in

inverse kinematics used as a surrogate for proton captures. With more intensive radioactive beams, more possibilities will arrive to study neutron captures; however, the single-particle structure is most pronounced closed to doubly magic nuclei such as $^{132}$Sn. Therefore, the method is not as useful for regions far from stability where collectivity is more pronounced.

#### 4.3.2.9 Experiments on Fission

Although fissioning nuclei of r-process interest have not yet been studied experimentally, many experiments provide essential data to test current fission models. The current status of fission and fission experiments has been reviewed in Ref. [144] and fission barriers of superheavy elements in Ref. [145]. In addition to these, there have been many measurements on fission yields for various fissioning systems using a Penning trap (see Sect. 4.3.2.1) as an ion counter (see, e.g., Refs. [146, 147]). The fission yield measurements are useful for testing the predictions from different fission models. They also provide information on isomeric yield ratios in fission.

## 4.4 Theory for Nuclear Astrophysics

### 4.4.1 Nuclear Masses

Among the ground-state properties, the atomic mass is obviously the most fundamental quantity. The calculation of the reaction cross section also requires the knowledge of other ground-state properties, such as the deformation, density distribution, or the single-particle-level scheme. When not available experimentally, these quantities need to be extracted from a mass model which aims at reproducing measured masses as accurately as possible, i.e., typically with a root-mean-square (rms) deviation of less than about 0.8 MeV. The importance of estimating all ground-state properties reliably should not be underestimated. For example, the nuclear level densities of a deformed nucleus at low energies (typically at the neutron separation energy) are predicted to be significantly (about 30–50 times) larger than those of a spherical one due principally to the rotational enhancement. An erroneous determination of the deformation can therefore lead to large errors in the estimate of radiative capture cross sections. For this reason, modern mass models not only try to reproduce at the best experimental masses and mass differences but also charge radii, quadrupole moments, giant resonances, fission barriers, shape isomers, infinite nuclear matter properties, . . . [148, 149].

With a view to their astrophysical application in neutron-rich environments, a series of nuclear-mass models have been developed based on the Hartree-Fock-Bogoliubov (HFB) method with Skyrme and contact-pairing forces, together with phenomenological Wigner terms and correction terms for the spurious collective energy within the cranking approximation (see Ref. [150] and references therein); all the model parameters have been fitted to essentially all the experimental mass data. While the first HFB-1 mass model aimed at proving that it was possible to reach a low rms deviation with respect to all experimental masses available at

that time, most of the subsequent models were developed to further explore the parameter space widely or to take into account additional constraints. These include in particular a sensitivity study of the mass model accuracy and extrapolation to major changes in the description of the pairing interaction, the spin-orbit coupling, or the nuclear matter properties, such as the effective mass, the symmetry energy, and the stability of the equation of state.

With respect to the 2457 measured masses for $Z, N \geq 8$ nuclei [21], the 32 HFB mass models give an rms deviation ranging between 0.52 MeV for HFB-27 and 0.82 MeV for HFB-1. These rms deviations can be compared to those obtained with other global mass models, such as the Gogny-HFB mass model with the D1M interaction [151] characterized by an rms of 0.81 MeV or the 2012 version of the finite-range droplet model [152] with 0.61 MeV. However, when dealing with exotic nuclei far away from stability, deviations between the HFB mass predictions can become significant, not only in the rigidity of the mass parabola but also in the description of the shell gaps or pairing correlations [153]. The $1\sigma$ variance between the 32 HFB mass predictions (with respect to the HFB-24 mass model) is illustrated in Fig. 4.11 where deviations up to about 3 MeV can be found at the neutron drip line for the heaviest species. Such uncertainties can be interpreted as the model uncertainties (due to model defects) inherent to the given HFB model [154]. These model uncertainties have been shown to be significantly larger than the uncertainties associated with local variations of the model parameters in the vicinity of an HFB minimum [153], as estimated using a variant of the Backward-Forward Monte Carlo method [155] to propagate the uncertainties on the masses of exotic nuclei far away

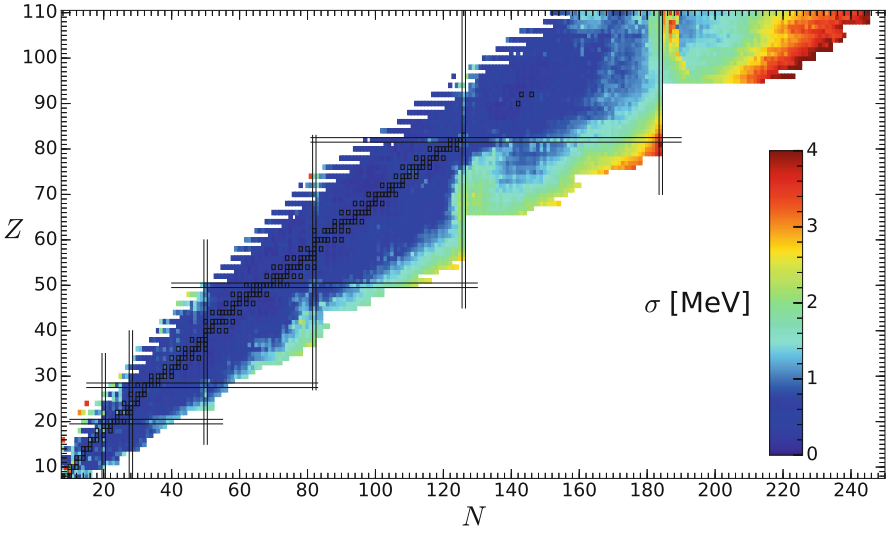


**Fig. 4.11** Representation in the $(N, Z)$ plane of the $1\sigma$ uncertainty corresponding to the 32 Skyrme-HFB mass models (with respect to HFB-24) for all the 8500 nuclei included in the mass tables from $Z = 8$ up to $Z = 110$

from the experimentally known regions (note that in this method only parameter sets giving rise to masses in reasonable agreement with experiments for all known nuclei are considered).

Many effective interactions have been proposed to estimate nuclear structure properties within the relativistic or non-relativistic mean-field approaches [156]. Except the BSk forces at the origin of the above-mentioned HFB mass models and the D1M interaction at the origin of the Gogny-HFB mass model [151], none of the others have been fitted to a large set of experimental masses. Consequently, their predictions lead to rms deviations typically larger than 2–3 MeV with respect to the bulk of known masses (e.g. masses obtained with the SLy4 force give an rms deviation of the order of 5 MeV [157]). With such a low accuracy, these masses should not be used for applications, such as the r-process nucleosynthesis. Additionally, other global mass models have been developed, essentially within the macroscopic-microscopic approach [152, 158], but this approach remains unstable with respect to parameter variations, as shown in the framework of the droplet model in Ref. [69]. In addition, this approach suffers from major shortcomings, such as the incoherent link between the macroscopic part and the microscopic correction or the instability of the shell correction [148, 149]. For this reason, more fundamental approaches, such as the mean field, are needed for astrophysical applications.

When considering mass models obtained in relatively different frameworks, e.g., the Skyrme-HFB or Gogny-HFB mass models, still large deviations are found in the mass predictions away from the experimentally known region. For example, as shown in Fig. 4.12, deviations up to typically ±5 MeV can be observed for exotic nuclei between HFB-31 [150] and D1M [151] mass predictions, especially around

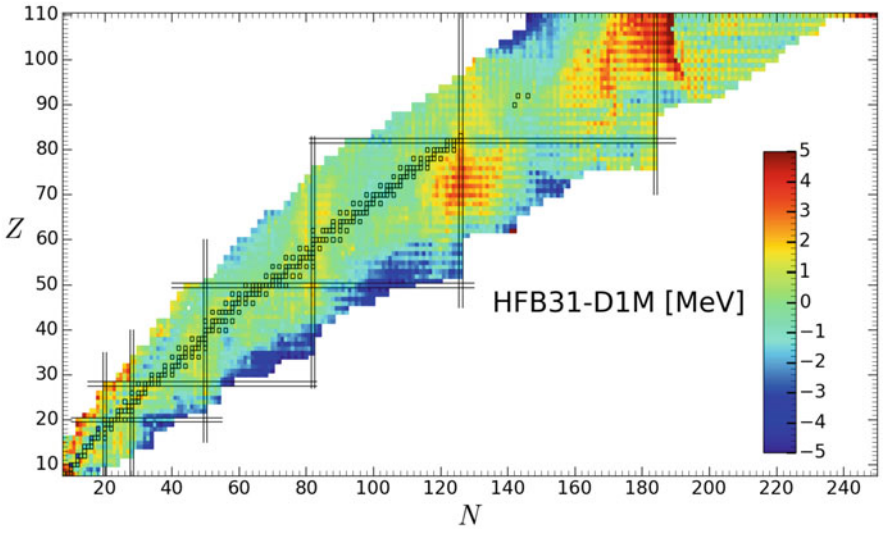


**Fig. 4.12** Representation in the $(N, Z)$ plane of the mass differences between HFB-31 [150] and D1M [151] models for all the 8500 nuclei from $Z = 8$ up to $Z = 110$

the $N = 126$ and 184 shell closures. Neutron-capture rates can consequently deviate by three to five orders of magnitude with such mass differences, essentially due to different local variations in the pairing and shell description (see Sect. 4.4.3). Such deviations by far exceed what is acceptable for nucleosynthesis applications. For this reason, further improvements of the mass model are required. These include development of relativistic as well as non-relativistic mean-field models but also the inclusion within such approaches of the state-of-the-art beyond-mean-field corrections, like the quadrupole or octupole correlations by the generator coordinate method [159, 160] and a proper treatment of odd-$A$ and odd-odd nuclei with time-reversal symmetry breaking. Such models should reproduce not only nuclear masses at best but also as many experimental observables as possible. These include charge radii and neutron skin thicknesses, fission barriers and shape isomers, spectroscopic data such as the $2^+$ energies, and moments of inertia but also infinite (neutron and symmetric) nuclear matter properties obtained from realistic calculations as well as specific observed or empirical properties of neutron stars, like their maximum mass or mass-radius relations [161, 162].

### 4.4.2 $\beta$-Decay Rates

$\beta$-decay rates play a fundamental role in nucleosynthesis in general [4] and more particularly for the r-process nucleosynthesis since they set the timescale of the nuclear flow and consequently of the production of the heavy elements. $\beta^-$-decay rates have been experimentally determined for 1213 nuclei [120] (see Sect. 4.3.2.7). For the few thousands nuclei missing in r-process nucleosynthesis simulations, only a restricted number of global models is available. These concern the macroscopic gross theory (GT2) [163], the FRDM+RPA [164], the Tamm-Dancoff approximation (TDA) [165], and the relativistic mean field plus QRPA (RMF+RRPA) [166]. Deviations between the predictions of some of these models are illustrated in Fig. 4.13 where ratios larger than a factor of 10 are found in many neutron-rich regions of the $(N,Z)$ plane, especially for heavy or superheavy nuclei.

Here also, more effort needs to be devoted to improve the prediction of $\beta$-decay rates, to include consistently not only the contribution of the forbidden transitions [166, 167] but also the deformation effects, the majority of nuclei being deformed [168, 169]. In particular, the first-forbidden transitions have been studied with the finite Fermi system theory [167] and the relativistic QRPA approach [166] but both only for spherical nuclei. Recent studies within the fully self-consistent proton-neutron QRPA model using the finite-range Gogny interaction have now also taken axially symmetric deformations into account [169], but forbidden transition remains to be included and the theory to be applied to systems with an odd number of nucleons. The inclusion of the phonon-phonon coupling has also been shown to give rise to a redistribution of the Gamow-Teller strength and impact the $\beta$-decay half-lives of neutron-rich nuclei significantly [170]. Further progress along all these lines will hopefully help improve the predictions. Finally, note that on the basis

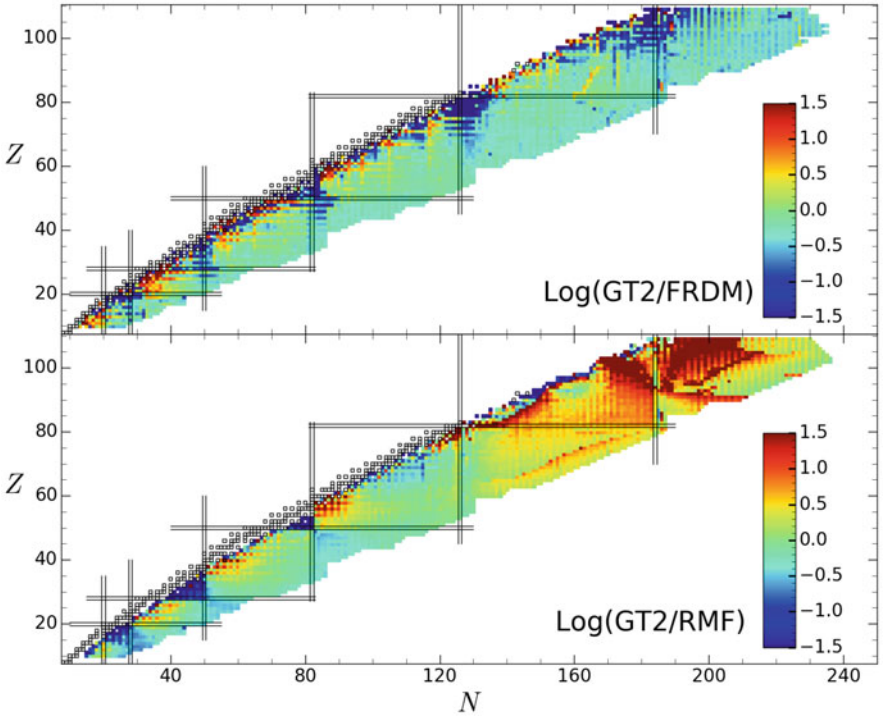


**Fig. 4.13** Representation in the $(N, Z)$ plane of the $\beta^-$-decay rate ratios (in log scale) obtained by three global models. *Upper panel*: Ratio between the HFB-21 + GT2 [163] and the FRDM+RPA rates [164]. *Lower panel*: Ratio between the HFB-21 + GT2 [163] and the RMF+RRPA rates [166]. The open squares correspond to the valley of $\beta$-stability. The double solid lines depict the neutron and proton magic numbers

of the $\beta$-decay strength, the $\beta$-delayed processes, including neutron emission and fission for the heaviest species, also need to be derived [70, 140].

### 4.4.3 Nuclear Reactions

Most of the low-energy cross-section calculations for nucleosynthesis applications are based on the statistical model of Hauser-Feshbach. Such a model makes the fundamental assumption that the capture process takes place with the intermediary formation of a compound nucleus in thermodynamic equilibrium. The energy of the incident particle is then shared more or less uniformly by all the nucleons before releasing the energy by particle emission or $\gamma$-de-excitation. The formation of a compound nucleus is usually justified by assuming that the level density in the compound nucleus at the projectile incident energy is large enough to ensure an average statistical continuum superposition of available resonances. The statistical

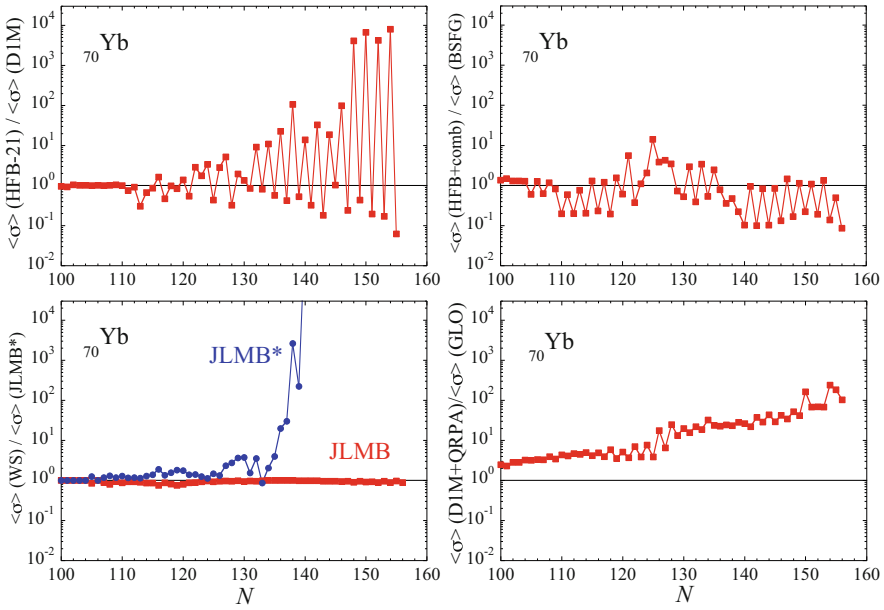


**Fig. 4.14** Illustration of some uncertainties affecting the prediction of the radiative neutron-capture rates for the Yb isotopes ($Z = 70$), between the valley of $\beta$-stability and the HFB-21 neutron drip line; these include the sensitivity to (*i*) the mass model when using the HFB-21 [183] or D1M [151] models (upper left), (*ii*) the nuclear level densities when using the HFB plus combinatorial [176] or the back-shifted Fermi gas (BSFG) [177] models (upper right), (*iii*) the optical potential adopting a Wood-Saxon (WS) potential [173] or two variants of the microscopic JLMB potentials [174, 175] (lower left), and (*iv*) the $\gamma$-ray strength function derived from either the D1M+QRPA [171] or the generalized Lorentzian (GLO) [184] models (lower right). The Maxwellian-averaged rates are estimated within the Hauser-Feshbach statistical model at $T = 10^9$ K

model has proven its ability to predict cross sections accurately for medium- and heavy-mass nuclei. However, this model suffers from uncertainties stemming essentially from the predicted nuclear ingredients describing the nuclear structure properties of the ground and excited states and the strong and electromagnetic interaction properties.

The impact of different input models adopted in the calculation of the reaction rates of astrophysical interest is illustrated in Fig. 4.14. Clear mass models have the strongest impact with deviation reaching four orders of magnitude for the most exotic neutron-rich nuclei. Nuclear level densities are seen to affect rates within typically a factor of 10 with a strong odd-even effect according to the way pairing interaction is treated. The $\gamma$-ray strength function may impact the prediction of the rate up to a factor of 100, in particular depending the way the low-energy tail of the giant $E1$ resonance is described, but also the low-energy $M1$ component is included, both for the scissors mode and for the so-called upbend [171, 172]. Finally, the optical potential is known to have a negligible impact in the standard

case (e.g. comparing the Woods-Saxon [173] and the microscopic so-called JLMB potential [174] in Fig. 4.14), although a reduction of the imaginary potential may have a drastic impact in reducing the absorption of neutrons by neutron-rich nuclei, as shown when considering the JLMB* potential [175]. More details on our capacity to predict reliably all these ingredients can be found in Refs. [4, 171, 175–178]. A review on the nuclear ingredients of relevance for the description of fission for nucleosynthesis applications and its fundamental role in r-process calculations can be found in Ref. [70].

When the number of available states in the compound nucleus is relatively small, the capture reaction is known to be possibly dominated by direct electromagnetic transitions to a bound final state rather than through a compound nucleus intermediary. It is now well accepted that this direct capture contribution is important and often dominant at the very low energies of astrophysical interest for light or exotic nuclei systems for which few or even no resonant states are available. The direct contribution to the neutron-capture rate can be two to three orders of magnitude larger than the one obtained within the Hauser-Feshbach approach traditionally used in nucleosynthesis applications [178–181]. Significant uncertainties still affect the direct capture predictions. These are related to the determination of the nuclear structure ingredients of relevance, i.e., the nuclear mass, spectroscopic factor, neutron-nucleus interaction potential, and excited level scheme. An important effort will have to be devoted to further improve the prediction of such nuclear inputs within reliable microscopic models, with a special emphasis on the determination of the low-energy excitation spectrum, in particular the spin and parity assignments. The transition from the compound nucleus to the direct capture mechanism, when only a few resonant states are available, also needs to be tackled in a more detailed way, for example, within the Breit-Wigner approach or the so-called high-fidelity-resonance technique [182].

## 4.5 Summary and Outlook

One of the major issues in modern astrophysics concerns the analysis of the present composition of the Universe and its various constituting objects. Nucleosynthesis models aim to explain the origin of the different nuclei observed in nature by identifying the possible processes able to synthesize them. Though the origin of most of the nuclides lighter than iron is now quite well understood, the synthesis of the heavy elements (i.e., heavier than iron) remains obscure in many respects, from the astrophysics as well as nuclear physics point of views. As far as nuclear physics is concerned, strong, weak, and electromagnetic interaction processes play an essential role in nucleosynthesis processes.

Radioactive beam facilities have provided new ways to explore key reactions for the nucleosynthesis of lighter elements. Many reactions have become available for studies in inverse kinematics using radioactive beams at astrophysically relevant energies. Surrogate reactions or $\beta$-delayed gamma and particle spectroscopy have provided information on the properties of key resonance states. On the other hand,

low-background facilities located underground have opened new possibilities to study reactions relevant for quiescent hydrogen and helium burning at or near astrophysically relevant energies.

For the synthesis of heavier elements, experiments at radioactive beam facilities have extended our knowledge of exotic nuclei and their properties, which serve as relevant inputs, for example, for the r-process calculations. Mass measurement techniques, such as Penning traps, MR-ToF mass spectrometers, and storage rings, have recently provided mass values for dozens of new neutron-rich nuclei. $\beta$-decay studies have yielded information on $\beta$-decay half-lives for several dozens of neutron-rich nuclei. Results on $\beta$-delayed neutron branchings obtained with the BRIKEN detector setup are coming and provide a major step forward in the knowledge of neutron-rich nuclei. Neutron-capture rates have been probed for specific nuclei using the $\beta$-Oslo method to determine the level densities and $\gamma$-ray strength functions. Several experiments have studied nuclear fission and fission yields, providing data to test various fission models. With anticipated new radioactive beam facilities, such as FRIB and FAIR, even more exotic nuclei will become available for experiments.

Although important effort has been devoted in the last decades to measure reaction cross sections, experimental data only covers a minute fraction of the whole set of data required for nuclear astrophysics applications. To fill the gaps, theoretical predictions are needed. Many astrophysics applications involve a large number of unstable nuclei and therefore require the use of global approaches. The extrapolation to exotic nuclei or energy ranges far away from experimentally known regions constrains the use of nuclear models to the most reliable ones, even if empirical approaches sometime present a better ability to reproduce experimental data. A subtle compromise between the reliability, accuracy, and applicability of the different theories available has to be found according to the specific application considered.

A continued effort to improve our predictions of the reaction and $\beta$-decay rates, including their statistical and systematic uncertainties, for nuclei far away from stability is obviously required. The reliability of our predictions today is still far from being at the level of the requirements in nuclear astrophysics applications. Priority should be given to a better description of the ground-state, fission, and $\beta$-decay properties but also nuclear level densities, optical potential, and $\gamma$-ray strength functions. A huge amount of work is still needed to make full advantage of the development of state-of-the-art microscopic models in building global universal models that include as much as possible the microscopic character of quantum physics. This effort to improve the microscopic nuclear predictions is concomitant with new development aiming at improving the description of the reaction mechanisms, including the equilibrium, pre-equilibrium, and direct capture processes. This theoretical work requires simultaneously new measurements of structure properties far away from stability but also reaction cross sections on stable targets and any experiments that can provide new insight on the numerous ingredients of the reaction models and their extrapolation far away from stability.

**Acknowledgments** SG acknowledges financial support from F.R.S.-FNRS (Belgium). This work has been supported by the Fonds de la Recherche Scientifique (F.R.S.-FNRS, Belgium) and the Research Foundation Flanders (FWO, Belgium) under the EOS Project nr O022818F. AK acknowledges financial support from the European Union's Horizon 2020 research and innovation program under Grant Agreement No. 771036 (ERC CoG MAIDEN).

## References

1. Y. Ivezić, T. Beers, M. Juric, et al., Ann. Rev. Astron. Astrophys. **50**, 251 (2012)
2. A.B.S. Reddy, D. Lambert, S. Giridhar, Mon. Notices Royal Astron. Soc. **463**, 4366 (2016)
3. B. Barbuy, C. Chiappini, O. Gerhard, Ann. Rev. Astron. Astrophys. **56**, 223 (2018)
4. M. Arnould, S. Goriely, Prog. Part. Nucl. Phys. **112**, 103766 (2020)
5. E. Anders, N. Grevesse, Geochim. Cosmochim. Acta **53**, 197 (1989)
6. M. Asplund, N. Grevesse, A.J. Sauval, P. Scott, Ann. Rev. Astron. Astrophys. **47**, 481 (2009)
7. K. Lodders, in *Principles and Perspectives in Cosmochemistry*, ed. by A. Goswami, B.E. Reddy (Springer Berlin Heidelberg, Berlin, Heidelberg, 2010), pp. 379–417
8. H. Palme, K. Lodders, A. Jones, Planets, Asteroids, Comets Solar Syst. **2**, 15 (2014)
9. S. Goriely, Astron. Astrophys. **342**(3), 881 (1999)
10. M. Arnould, S. Goriely, Phys. Rep. **384**, 1 (2003)
11. M. Arnould, S. Goriely, K. Takahashi, Phys. Rep. **450**, 97 (2007)
12. T. Lee, in *Meteorites and the Early Solar System*, ed. by J. Kerridge, M. Matthews (University of Arizona Press, Tucson, 1988), p. 1063
13. T. Swindle, in *Protostars and Planets III*, ed. by E. Levy, J. Lunine (University of Arizona Press, Tucson, 1993), p. 867
14. E. Anders, E. Zinner, Meteoritics **28**, 490 (1993)
15. E.M. Burbidge, G.R. Burbidge, W.A. Fowler, F. Hoyle, Rev. Mod. Phys. **29**, 547 (1957)
16. A.G.W. Cameron, Pub. Astron. Soc. Pac. **69**, 201 (1957)
17. V. Tatischeff, S. Gabici, Ann. Rev. Nucl. Part. Sci. **68**, 377 (2018)
18. S. Woosley, T. Weaver, Astrophys. J. Suppl. Ser. **101**, 181 (1995)
19. C. Iliadis, *Nuclear Physics of Stars*, 2nd edn. (Wiley-VCH, 2015)
20. M. Limongi, A. Chieffi, Astrophys. J. Suppl. Ser. **237**, 13 (2018)
21. M. Wang, W. Huang, F. Kondev, G. Audi, S. Naimi, Chin. Phys. C **45**(3), 030003 (2021)
22. F. Käppeler, H. Beer, K. Wisshak, Rep. Prog. Phys. **52**, 945 (1989)
23. S. Goriely, N. Mowlavi, Astron. Astrophys. **362**, 599 (2000)
24. A.I. Karakas, J.C. Lattanzio, Pub. Astron. Soc. Pac. **31**, e030 (2014)
25. S. Goriely, L. Siess, Astron. Astrophys. **609**, A29 (2018)
26. G. Meynet, S. Ekström, A. Maeder, Astron. Astrophys. **447**, 623 (2006)
27. U. Frischknecht, R. Hirschi, M. Pignatari, et al., Mon. Notices Royal Astron. Soc. **456**, 1803 (2016)
28. A. Choplin, R. Hirschi, G. Meynet, S. Ekström, C. Chiappini, A. Laird, Astron. Astrophys. **618**, A133 (2018)
29. J. Cowan, C. Sneden, J. Lawler, A. Aprahamian, M. Wiescher, K. Langanke, G. Martínez-Pinedo, F.K. Thielemann, Rev. Mod. Phys. **93**, 015002 (2021)
30. H.T. Janka, *Handbook of Supernovae* (Springer International Pub. AG, 2017)
31. S. Wanajo, B. Müller, H.T. Janka, A. Heger, Astrophys. J **853**, 40 (2018)
32. H.T. Janka, Ann. Rev. Nucl. Part. Sci. **62**, 407 (2012)
33. H.T. Janka, T. Melson, A. Summa, Ann. Rev. Nucl. Part. Sci. **66**, 341 (2016)
34. N. Nishimura, T. Takiwaki, F.K. Thielemann, Astrophys. J **810**, 109 (2015)
35. D. Siegel, J. Barnes, B. Metzger, Nature **569**, 241 (2019)
36. O. Just, I. Kullmann, S. Goriely, A. Bauswein, H.T. Janka, C.E. Collins, Mon. Notices Royal Astron. Soc., submitted (2021). [arXiv]:2109.14617 [astro-ph.HE]

37. C. Winteler, R. Käppeli, A. Perego, A. Arcones, N. Vasset, N. Nishimura, M. Liebendörfer, F.K. Thielemann, Astrophys. J **750**, L22 (2012)
38. L. Roberts, D. Kasen, W. Lee, E. Ramirez-Ruiz, Astrophys. J. Lett. **736**, L21 (2011)
39. S. Goriely, A. Bauswein, H.T. Janka, Astrophys. J. Lett. **738**, L32 (2011)
40. O. Just, A. Bauswein, R. Ardevol Pulpillo, S. Goriely, H.T. Janka, Mon. Notices Royal Astron. Soc. **448**, 541 (2015)
41. A. Bauswein, R. Ardevol Pulpillo, H.T. Janka, S. Goriely, Astrophysical J. Lett. **773**, L9 (2014)
42. S. Wanajo, Y. Sekiguchi, N. Nishimura, K. Kiuchi, K. Kyutoku, M. Shibata, Astrophys. J. Lett. **789**, L39 (2014)
43. B. Abbott, R. Abbott, T. Abbott, et al., Phys. Rev. Lett. **119**, 161101 (2017)
44. D. Watson, C.J. Hansen, J. Selsing, A. Koch, D.B. Malesani, et al., Nature **574**, 497 (2019)
45. S. Goriely, A. Bauswein, O. Just, E. Pllumbi, H.T. Janka, Mon. Notices Royal Astron. Soc. **452**, 3894 (2015)
46. R. Ardevol-Pulpillo, H.T. Janka, O. Just, A. Bauswein, Mon. Notices Royal Astron. Soc. **485**, 4754 (2019)
47. V. Nedora, S. Bernuzzi, D. Radice, B. Daszuta, A. Endrizzi, A. Perego, A. Prakash, M. Safarzadeh, F. Schianchi, D. Logoteta, Astrophys. J **906**, 98 (2021)
48. F. Herwig, M. Pignatari, P.R. Woodward, D.H. Porter, G. Rockefeller, C.L. Fryer, M. Bennett, R. Hirschi, Astrophys. J **727**, 89 (2011)
49. M. Hampel, R.J. Stancliffe, M. Lugaro, B.S. Meyer, Astrophys. J **831**, 171 (2016)
50. O. Clarkson, F. Herwig, M. Pignatari, Mon. Notices Royal Astron. Soc. **474**, L37 (2018)
51. P.A. Denissenkov, F. Herwig, P. Woodward, R. Andrassy, M. Pignatari, S. Jones, Mon. Notices Royal Astron. Soc. **488**(3), 4258 (2019)
52. A. Choplin, L. Siess, S. Goriely, Astron. Astrophys. **648**, A119 (2021)
53. S. Goriely, L. Siess, A. Choplin, Astron. Astrophys. **654**, A129 (2021)
54. M. Rayet, M. Arnould, M. Hashimoto, et al., Astron. Astrophys. **298**, 517 (1995)
55. C. Travaglio, T. Rauscher, A. Heger, M. Pignatari, C. West, Astrophys. J **854**, 18 (2018)
56. K. Nomoto, F.K. Thielemann, K. Yokoi, Astrophys. J **286**, 644 (1984)
57. W. Hillebrandt, J. Niemeyer, Ann. Rev. Astron. Astrophys. **38**, 191 (2000)
58. C. Travaglio, R. Gallino, T. Rauscher, F. Röpke, W. Hillebrandt, Astrophys. J. **799**, 54 (2015)
59. S. Goriely, D. Garcia-Senz, E. Bravo, J. José, Astron. Astrophys. **444**, L1 (2005)
60. C. Fröhlich, G. Martínez-Pinedo, M. Liebendörfer, F.K. Thielemann, E. Bravo, W.R. Hix, K. Langanke, N.T. Zinner, Phys. Rev. Lett. **96**, 142502 (2006)
61. K. Takahashi, K. Yokoi, At. Data Nucl. Data Tables **36**, 375 (1987)
62. C. Iliadis, A. Champagne, A. Chieffi, M. Limongi, Astrophys. J. Suppl. Ser. **193**(1), 16 (2011)
63. R.C. Runkle, A.E. Champagne, J. Engel, Astrophys. J. **556**(2), 970 (2001)
64. S.S. Gupta, B.S. Meyer, Phys. Rev. C **64**, 025805 (2001)
65. G.W. Misch, S.K. Ghorui, P. Banerjee, Y. Sun, M.R. Mumpower, Astrophys. J. Suppl. Ser. **252**(1), 2 (2020)
66. D. Yakovlev, L.R. Gasques, A.V. Afanasjev, et al., Phys. Rev. C **74**, 035803 (2006)
67. A. Potekhin, G. Chabrier, Contrib. Plasma Phys. **53**, 397 (2013)
68. Y. Génolini, D. Maurin, I.V. Moskalenko, M. Unger, Phys. Rev. C **98**, 034611 (2018)
69. S. Goriely, M. Arnould, Astron. Astrophys. **262**, 73 (1992)
70. S. Goriely, Eur. Phys. J. A **51**, 22 (2015)
71. S. Goriely, G. Martínez-Pinedo, Nucl. Phys. A **944**, 158 (2015)
72. J.F. Lemaître, S. Goriely, A. Bauswein, H.T. Janka, Phys. Rev. C **103**, 025806 (2021)
73. M. Aliotta, R. Buompane, M. Couder, A. Couture, R. deBoer, A. Formicola, et al., J. Phys. G: Nucl. Part. Phys. **49**, 010501 (2021)
74. R. Reifarth, C. Lederer, F. Käppeler, J. Phys. G: Nucl. Part. Phys. **41**(5), 053101 (2014)
75. R. Diehl, H. Halloin, K. Kretschmer, G.G. Lichti, V. Schönfelder, A.W. Strong, et al., Nature **439**(7072), 45 (2006)
76. L. Buchmann, M. Hilgemeier, A. Krauss, A. Redder, C. Rolfs, H. Trautvetter, T. Donoghue, Nucl. Phys. A **415**(1), 93 (1984)

77. C. Ruiz, A. Parikh, J. José, L. Buchmann, J.A. Caggiano, A.A. Chen, J.A. Clark, H. Crawford, B. Davids, J.M. D'Auria, C. Davis, C. Deibel, L. Erikson, L. Fogarty, D. Frekers, U. Greife, A. Hussein, D.A. Hutcheon, M. Huyse, C. Jewett, A.M. Laird, R. Lewis, P. Mumby-Croft, A. Olin, D.F. Ottewell, C.V. Ouellet, P. Parker, J. Pearson, G. Ruprecht, M. Trinczek, C. Vockenhuber, C. Wrede, Phys. Rev. Lett. **96**, 252501 (2006)
78. R. Dressler, M. Ayranov, D. Bemmerer, M. Bunka, Y. Dai, et al., J. Phys. G: Nucl. Part. Phys. **39**(10), 105201 (2012)
79. V. Margerin, A. Murphy, T. Davinson, R. Dressler, J. Fallis, et al., Phys. Lett. B **731**, 358 (2014)
80. B.W. Grefenstette, F.A. Harrison, S.E. Boggs, S.P. Reynolds, C.L. Fryer, et al., Nature **506**(7488), 339 (2014)
81. M. Renaud, J. Vink, A. Decourchelle, F. Lebrun, P.R. den Hartog, et al., Astrophys. J. **647**(1), L41 (2006)
82. S.A. Grebenev, A.A. Lutovinov, S.S. Tsygankov, C. Winkler, Nature **490**, 373 (2012)
83. A. Kankainen, P.J. Woods, F. Nunes, C. Langer, H. Schatz, et al., Eur. Phys. J. A **52**(1), 6 (2016)
84. R.B. Vogelaar, L.W. Mitchell, R.W. Kavanagh, A.E. Champagne, P.V. Magnus, M.S. Smith, A.J. Howard, P.D. Parker, H.A. O Brien, Phys. Rev. C **53**, 1945 (1996)
85. A. Kankainen, P.J. Woods, H. Schatz, T. Poxon-Pearson, D.T. Doherty, et al., Phys. Lett. B **769**, 549 (2017)
86. D. Kahl, P.J. Woods, T. Poxon-Pearson, F.M. Nunes, B.A. Brown, H. Schatz, et al., Phys. Lett. B **797**, 134803 (2019)
87. M.B. Bennett, C. Wrede, B.A. Brown, S.N. Liddick, D. Pérez-Loureiro, et al., Phys. Rev. Lett. **116**, 102502 (2016)
88. C. Iliadis, Phys. Rev. C **99**, 065809 (2019)
89. L.S. Brown, G. Gabrielse, Phys. Rev. A **25**, 2423 (1982)
90. L.S. Brown, G. Gabrielse, Rev. Mod. Phys. **58**, 233 (1986)
91. G. Gräff, H. Kalinowsky, J. Traut, Z. Phys. A **297**(1), 35 (1980)
92. M. König, G. Bollen, H.J. Kluge, T. Otto, J. Szerypo, Int. J. Mass Spectrom. Ion Proc. **142**(1–2), 95 (1995)
93. S. George, K. Blaum, F. Herfurth, A. Herlert, M. Kretzschmar, S. Nagy, S. Schwarz, L. Schweikhard, C. Yazidjian, Int. J. Mass Spectrom. **264**(2–3), 110 (2007)
94. M. Kretzschmar, Int. J. Mass Spectrom. **264**(2–3), 122 (2007)
95. M. Vilen, J.M. Kelly, A. Kankainen, M. Brodeur, et al., Phys. Rev. C **101**, 034312 (2020)
96. S. Eliseev, K. Blaum, M. Block, C. Droese, M. Goncharov, et al., Phys. Rev. Lett. **110**, 082501 (2013)
97. S. Eliseev, K. Blaum, M. Block, A. Dörr, C. Droese, et al., Appl. Phys. B **114**(1), 107 (2014)
98. O.T. Kaleja, Ph.D. thesis, Johannes Gutenberg-Universität Mainz (2020)
99. M.B. Comisarow, A.G. Marshall, Chem. Phys. Lett. **25**(2), 282 (1974)
100. T. Eronen, A. Kankainen, J. Äystö, Progr. Part. Nucl. Phys. **91**, 259 (2016)
101. J. Dilling, K. Blaum, M. Brodeur, S. Eliseev, Ann. Rev. Nucl. Part. Sci. **68**, 45 (2018)
102. H. Wollnik, Int. J. Mass Spectrom. **349–350**, 38 (2013)
103. R. Wolf, F. Wienholtz, et al., Int. J. Mass Spectrom. **349–350**, 123 (2013)
104. W.R. Plaß, T. Dickel, C. Scheidenberger, Int. J. Mass Spectrom. **349–350**, 134 (2013)
105. T. Dickel, W. Plaß, et al., Nucl. Instrum. Methods Phys. Res. Sect. A **777**, 172 (2015)
106. M. Reiter, S.A.S. Andrés, J. Bergmann, T. Dickel, J. Dilling, et al., Nucl. Instrum. Methods Phys. Res. Sect. A **1018**, 165823 (2021)
107. V. Manea, J. Karthein, D. Atanasov, M. Bender, K. Blaum, et al., Phys. Rev. Lett. **124**, 092502 (2020)
108. M. Steck, Y.A. Litvinov, Progr. Part. Nucl. Phys. **115**, 103811 (2020)
109. B. Franzke, H. Geissel, G. Münzenberg, Mass Spectrom. Rev. **27**(5), 428 (2008)
110. J. Xia, W. Zhan, B. Wei, Y. Yuan, M. Song, et al., Nucl. Instrum. Methods Phys. Res. A (1), 11 (2002)
111. Y.H. Zhang, Y.A. Litvinov, T. Uesaka, H.S. Xu, Phys. Scripta **91**(7), 073002 (2016)

112. B. Mei, T. Aumann, S. Bishop, K. Blaum, K. Boretzky, et al., Phys. Rev. C **92**, 035803 (2015)
113. J. Glorius, C. Langer, Z. Slavkovská, L. Bott, C. Brandau, et al., Phys. Rev. Lett. **122**, 092701 (2019)
114. Y.H. Zhang, P. Zhang, X.H. Zhou, M. Wang, Y.A. Litvinov, et al., Phys. Rev. C **98**, 014319 (2018)
115. A. Estradé, M. Matoš, H. Schatz, et al., Phys. Rev. Lett. **107**, 172503 (2011)
116. Z. Meisel, S. George, et al., Phys. Rev. Lett. **114**, 022501 (2015)
117. Z. Meisel, S. George, S. Ahn, et al., Phys. Rev. Lett. **115**, 162501 (2015)
118. Z. Meisel, S. George, et al., Phys. Rev. C **101**, 052801 (2020)
119. W. Huang, M. Wang, F. Kondev, G. Audi, S. Naimi, Chin. Phys. C **45**(3), 030002 (2021)
120. F.G. Kondev, M. Wang, W.J. Huang, S. Naimi, G. Audi, Chin. Phys. C **45**(3), 030001 (2021)
121. T. Eronen, et al., Eur. Phys. J. A **48**(4), 46 (2012)
122. M. Vilen, J.M. Kelly, A. Kankainen, M. Brodeur, et al., Phys. Rev. Lett. **120**, 262701 (2018)
123. D. Atanasov, P. Ascher, K. Blaum, R.B. Cakirli, T.E. Cocolios, et al., Phys. Rev. Lett. **115**, 232501 (2015)
124. M.P. Reiter, S. Ayet San Andrés, S. Nikas, J. Lippuner, et al., Phys. Rev. C **101**, 025803 (2020)
125. L. Canete, S. Giraud, A. Kankainen, B. Bastin, F. Nowacki, A. Poves, et al., Phys. Rev. C **101**, 041304 (2020)
126. Z.Y. Xu, S. Nishimura, G. Lorusso, F. Browne, P. Doornenbal, et al., Phys. Rev. Lett. **113**, 032505 (2014)
127. G. Lorusso, S. Nishimura, Z.Y. Xu, A. Jungclaus, Y. Shimizu, et al., Phys. Rev. Lett. **114**, 192501 (2015)
128. R. Caballero-Folch, C. Domingo-Pardo, J. Agramunt, A. Algora, F. Ameil, et al., Phys. Rev. Lett. **117**, 012501 (2016)
129. R. Caballero-Folch, C. Domingo-Pardo, J. Agramunt, A. Algora, F. Ameil, et al., Phys. Rev. C **95**, 064322 (2017)
130. J. Wu, S. Nishimura, G. Lorusso, P. Möller, E. Ideguchi, et al., Phys. Rev. Lett. **118**, 072701 (2017)
131. M. Piersa-Siłkowska, A. Korgul, et al., Phys. Rev. C **104**, 044328 (2021)
132. R.B. Roberts, L.R. Hafstad, R.C. Meyer, P. Wang, Phys. Rev. **55**, 664 (1939)
133. R.E. Azuma, L.C. Carraz, P.G. Hansen, B. Jonson, K.L. Kratz, et al., Phys. Rev. Lett. **43**, 1652 (1979)
134. R. Azuma, T. Björnstad, H. Gustafsson, P. Hansen, B. Jonson, S. Mattsson, G. Nyman, A. Poskanzer, H. Ravn, Phys. Lett. B **96**(1), 31 (1980)
135. J. Dufour, R. Del Moral, F. Hubert, D. Jean, M. Pravikoff, et al., Phys. Lett. B **206**(2), 195 (1988)
136. J. Agramunt, J. Tain, M. Gómez-Hornillos, A. Garcia, F. Albiol, et al., Nucl. Instrum. Methods Phys. Res. A **807**, 69 (2016)
137. I.D. Moore, et al., Nucl. Instrum. Methods Phys. Res. B **317**, 208 (2013)
138. R. Caballero-Folch, I. Dillmann, J. Agramunt, J.L. Taín, A. Algora, et al., Phys. Rev. C **98**, 034310 (2018)
139. A. Tolosa-Delgado, J. Agramunt, J.L. Tain, A. Algora, C. Domingo-Pardo, et al., Nucl. Instrum. Methods Phys. Res. A **925**, 133 (2019)
140. P. Dimitriou, I. Dillmann, B. Singh, V. Piksaikin, K. Rykaczewski, J. Tain, et al., Nucl. Data Sheets **173**, 144 (2021)
141. A. Spyrou, S.N. Liddick, A.C. Larsen, M. Guttormsen, et al., Phys. Rev. Lett. **113**, 232502 (2014)
142. S.N. Liddick, A. Spyrou, B.P. Crider, F. Naqvi, A.C. Larsen, et al., Phys. Rev. Lett. **116**, 242502 (2016)
143. K.L. Jones, A.S. Adekola, D.W. Bardayan, J.C. Blackmon, K.Y. Chae, K.A. Chipps, J.A. Cizewski, L. Erikson, C. Harlin, R. Hatarik, et al., Nature **465**(7297), 454 (2010)
144. A.N. Andreyev, K. Nishio, K.H. Schmidt, Rep. Progr. Phys. **81**(1), 016301 (2017)
145. F.P. Heßberger, Eur. Phys. J. A **53**, 75 (2017)
146. H. Penttilä, D. Gorelov, et al., Eur. Phys. J. A **52**, 104 (2016)

147. V. Rakopoulos, M. Lantz, S. Pomp, A. Solders, A. Al-Adili, et al., Phys. Rev. C **99**, 014617 (2019)
148. J.M. Pearson, Hyperfine Interact. **132**, 59 (2001)
149. D. Lunney, J. Pearson, C. Thibault, Rev. Mod. Phys. **75**(3), 1021 (2003)
150. S. Goriely, N. Chamel, J.M. Pearson, Phys. Rev. C **93**, 034337 (2016)
151. S. Goriely, S. Hilaire, M. Girod, S. Péru, Phys. Rev. Lett. **102**, 242501 (2009)
152. P. Möller, A. Sierk, T. Ichikawa, H. Sagawa, At. Data Nucl. Data Tables **109–110**, 1 (2016)
153. S. Goriely, R. Capote, Phys. Rev. C **89**, 054318 (2014)
154. D. Neudecker, R. Capote, H. Leeb, Nucl. Instrum. Methods Phys. Res. A **723**, 163 (2013)
155. E. Bauge, P. Dossantos-Uzarralde, J. Korean Phys. Soc. **59**, 1218 (2011)
156. M. Bender, P.H. Heenen, P.G. Reinhard, Rev. Mod. Phys. **75**, 121 (2003)
157. M. Stoitsov, J. Dobaczewski, W. Nazarewicz, S. Pittel, D. Dean, Phys. Rev. C **68**, 054312 (2003)
158. N. Wang, M. Liu, X. Wu, J. Meng, Phys. Lett. B **734**, 215 (2014)
159. M. Bender, G. Bertsch, P.H. Heenen, Phys. Rev. C **73**, 034322 (2006)
160. L. Robledo, T. Rodríguez, R. Rodríguez-Guzmán, J. Phys. G: Nucl. Part. Phys. **46**, 013001 (2018)
161. A.F. Fantina, N. Chamel, J.M. Pearson, S. Goriely, Astron. Astrophys. **559**, A128 (2013)
162. J.M. Pearson, N. Chamel, A.Y. Potekhin, A.F. Fantina, C. Ducoin, A.K. Dutta, S. Goriely, Mon. Notices Royal Astron. Soc. **481**(3), 2994 (2018)
163. T. Tachibana, M. Yamada, Y. Yoshida, Prog. Theor. Phys. **84**, 641 (1990)
164. P. Möller, B. Pfeiffer, K.L. Kratz, Phys. Rev. C **67**, 055802 (2003)
165. H. Klapdor, J. Metzinger, T. Oda, At. Data Nuc. Data Tables **31**, 81 (1984)
166. T. Marketin, L. Huther, G. Martinez-Pinedo, Phys. Rev. C **93**, 025805 (2016)
167. I. Borzov, Phys. Part. Nuclei **48**, 885 (2017)
168. J.M. Boillos, P. Sarriguren, Phys. Rev. C **91**, 034311 (2015)
169. M. Martini, S. Péru, S. Goriely, Phys. Rev. C **89**, 044306 (2014)
170. A.P. Severyukhin, V.V. Voronov, I.N. Borzov, N.N. Arsenyev, N.V. Giai, Phys. Rev. C **90**, 044320 (2014)
171. S. Goriely, S. Hilaire, S. Péru, K. Sieja, Phys. Rev. C **98**, 014327 (2018)
172. S. Goriely, P. Dimitriou, M. Wiedeking, et al., Eur. Phys. J. A **55**, 172 (2019)
173. A. Koning, J. Delaroche, Nucl. Phys. A **713**(3–4), 231 (2003)
174. J. Jeukenne, A. Lejeune, C. Mahaux, Phys. Rev. C **16**, 80 (1977)
175. S. Goriely, J.P. Delaroche, Phys. Lett. B **653**, 178 (2007)
176. S. Goriely, S. Hilaire, A.J. Koning, Phys. Rev. C **78**, 064307 (2008)
177. A. Koning, S. Hilaire, S. Goriely, Nucl. Phys. A **810**, 13 (2008)
178. S. Goriely, Eur. Phys. J. A **51**, 172 (2015)
179. Y. Xu, S. Goriely, Phys. Rev. C **86**, 045801 (2012)
180. Y. Xu, S. Goriely, A.J. Koning, S. Hilaire, Phys. Rev. C **90**, 024604 (2014)
181. K. Sieja, S. Goriely, Eur. Phys. J. A **57**, 110 (2021)
182. D. Rochman, S. Goriely, A. Koning, H.Ferroukhi, Phys. Lett. B **764**, 109 (2017)
183. S. Goriely, N. Chame, J. Pearson, Phys. Rev. C **82**, 035804 (2010)
184. J. Kopecky, M. Uhl, Phys. Rev. C **41**, 1941 (1990)